ABSTRACT

Title of Thesis:	DATA-DRIVEN DESIGN OF MXENE AEROGELS WITH PROGRAMMABLE MECHANICAL PERFORMANCE VIA ACTIVE LEARNING AND COLLABORATIVE ROBOTS
	Snehi Shrestha, Master of Science, 2022
Thesis Directed By:	Prof. Po-Yen Chen, Department of Chemical & Biomolecular Engineering

There is a solid demand for developing intelligent pressure sensing materials for the next generation of soft machines and robots. The piezoresistive pressure sensor requires a high sensitivity within a specific pressure range and possesses superior mechanical stability. $Ti_3C_2T_x$ MXene-based aerogels with high electrical conductivities have been demonstrated as promising piezoresistive materials for the fabrication of intelligent pressure sensors for diverse sensing applications, from ultra-low stress vibration detection to irregular object grasping. MXene aerogels' piezoresistive behaviors can easily be tuned by changing the fabrication recipes that affect micro/nanostructures. Although many techniques have been reported for fabricating MXene aerogels for specific detection limits, the influence of the interplaying factors and their effect on the aerogels' structures and mechanical properties are not clearly understood. To achieve the custom design for pressure sensors for any given sensing windows and mechanical requirements,

understanding the complex correlations between fabrication recipes, aerogel microstructures, and mechanical properties becomes necessary.

Since traditional trial-and-error approaches require the production and manual processing of a large amount of data and, therefore, are highly time-consuming. Also, it is impossible to use a trial-and-error-based approach to study multi-dimensional design space as the one needed to construct an enormous amount of MXene-based aerogel sensors. Machine learning is a powerful and versatile tool that uses data-driven computation to uncover underlying trends and complex correlations. Machine learning requires a data-rich system to study the correlations and make accurate analyses and predictions. As the quality and size of the data obtained from the literature remain narrow and biased, it becomes essential to design high-throughput experiments to supply high-quality data to develop prediction models via machine learning. In this presentation, we adopt a hybrid strategy using wet-lab experiments, a machine learning framework, and collaborative robot assistance to build up a prediction model and uncover the underlying design principles to understand the mechanical properties of MXene-based aerogel sensors.

Three functional materials (i.e., $Ti_3C_2T_x$ MXene nanosheets, cellulose nanofibers, and gelatin), and one crosslinker (i.e., glutaraldehyde), are used for the fabrication of piezoresistive aerogels. First, a support-vector machine classifier is trained with 264 different compositions to confirm a feasible fabrication regime. Second, 160 piezoresistive aerogels with various recipes and morphologies are fabricated through active learning loops. Third, through data analyses, data-driven design principles for piezoresistive aerogels were uncovered and validated via in situ microscopic studies. Through this study, we make a crucial discovery about the roles of mass loading and cellulose nanofiber concentration on the mechanical properties of the resulting

aerogels. Finally, we demonstrate how the implementation of collaborative robots can accelerate the prediction model construction.

DATA-DRIVEN DESIGN OF MXENE AEROGELS WITH PROGRAMMABLE MECHANICAL PERFORMANCE VIA ACTIVE LEARNING AND COLLABORATIVE ROBOTS

by

Snehi Shrestha

Thesis submitted to the Faculty of the Graduate School of the
University of Maryland, College Park, in partial fulfillment
of the requirements for the degree of
Master of Science
2022

Advisory Committee:
Prof. Po-Yen Chen, Chair
Prof. Peter Kofinas
Prof. Srinivasa R. Raghavan
Prof. Taylor J. Woehl
Prof. Arthur Yang

Dedication

This is dedicated to my family – Mom, Baba, Samridhi, and the rest of the bunch. Thank you for being there for me for the most trying of times. Thank you for all the home-made food, lodging, love, care, and support without which I could not have complete this thesis.

Acknowledgements

First, I want to express my deepest gratitude to my advisor, Dr. Po-Yen Chen, for allowing me to work on this project. His vision, insight, and guidance have been a constant support, without which I could not have completed this thesis.
I would also like to thank my committee members- Dr. Peter Kofinas, Dr. Srinivasa R. Raghavan, Dr. Taylor J. Woehl, and Dr. Arthur Yang for lending me their valuable time and agreeing to serve on my committee.

Next, I want to thank my lab members - Tinale Chen, Shuaiming He, Meera Kesavan, Joshua Little, and Haochen Yang, for answering my numerous questions, for showing me the ropes, for their kind support, and for their words of encouragement when I needed them the most.

I want to thank the undergraduate student I worked with this past two years – Christopher Hawkins Cooney, Isabella Rose Burdelas, Ari Micah Sporkin, and Manasvi Chegu, for their indispensable role in completing this thesis.

I also want to thank Dr. Sz-Chian Liou for helping me with countless SEM (Scanning Electron Microscopy) sessions.

Lastly, I want to thank my friends and family for making me believe in hard work and for being tremendous support this entire time.

Table of Contents

List of Figures

Chapter 1: Introduction

1.1 Background -MXene

Ever since Novoselov, Geim, and coworkers were able to exfoliate graphene from graphite successfully, there has been a surge in the research interest to discover, understand and apply other similar kinds of two-dimensional (2D) nanomaterials. Ultrathin 2D nanomaterials have lateral sizes larger than 100 nm, but their thickness is only about one to a few atoms thick. [1] Graphene is an ultrathin 2D nanomaterial that is only an atom thick where the carbon atoms are packed in a tight hexagonal crystalline form. This structure of graphene bonds carbon atoms in strong in-plane covalent bonds, which provide the material with extraordinary mechanical strength with the Young's Modulus of 1.0 TPa.[2] Moreover, the ability of graphene to confine clouds of electrons over the hexagons of carbon atoms gives it superb electrical and thermal conductivity. [1] Furthermore, graphene also exhibits complex and intriguing behavior that directly correlates with the number of layers present in its structure. Single and double-layered graphene behaves as a zero-bandgap semi-metal. Whereas, for graphene with 3 to 10 layers that are stacked together, their conduction and valence bands overlap. [3]

The success of graphene has led to the discovery of other ultrathin 2D nanomaterials such as transition metal dichalcogenides (TMDs), transition metal oxides (TMOs), black phosphorus (BP), hexagonal boron nitride (h-BN), boron nanosheets (B NSs) and tin telluride nanosheets (SnTe NSs) to name a few. [4] These ultrathin 2D nanomaterials have large aspect ratios, which endow them with sheet-like structures.[1] Similarly, MXene is another example of ultrathin 2D nanomaterials,

discovered at Drexel University in 2011 by Naguib et al. [5] MXene represents a burgeoning group of ultrathin 2D nanomaterials that consists of carbides or nitrides of early transition metal. Their stoichiometric composition follows this general formula - $M_{n+1}X_nT_x$, where M represents a d group transition metal, X represents carbon or nitrogen, and T means surface terminal groups (-O, -OH, F and Cl).[6] In 2D MXene, the X_n layers are interlaid between the M_{n+1} layers.[6]

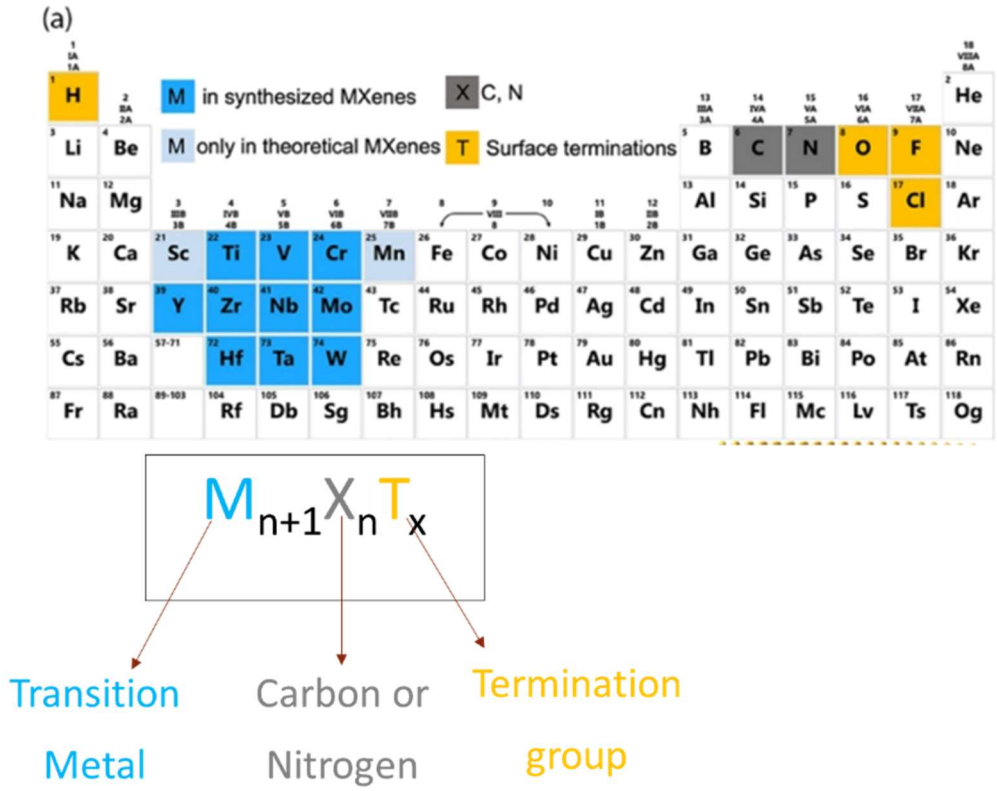

Figure 1. General stoichiometric formula of MXenes and elements in the periodic table that can be used to form MXenes [6]

1.2 MXene Synthesis and characterization

MXenes are derived from their parental MAX phases, which are a family of the layered ternary system material consisting of transition metal, metalloid, and carbon or

nitrogen in a hexagonal structure.[7-10] The formula for MAX's stoichiometric composition is $M_{n+1}AX_n$, where M is the transition metal, A is a Group 13 or Group 14 element, and X is carbon or nitrogen.[6] They display a unique combination of ceramic and metallic behavior.[8] In MAX, the M-X bonds tend to be stronger than the M-A bonds because whereas M-X bonds have metallic, covalent, and ionic characteristics, M-A bonds are purely metallic.[8] Therefore, the A layer can be selectively etched out through chemical exfoliation resulting in 2D exfoliated $M_{n+1}X_n$ nanosheets (Figure 2) covered with terminating groups derived from the etchant.[9] While there are other methods to synthesize MXene, the "top-down" route of selective etching of MAX phases remains a dominant method to form MXene.[9,11]

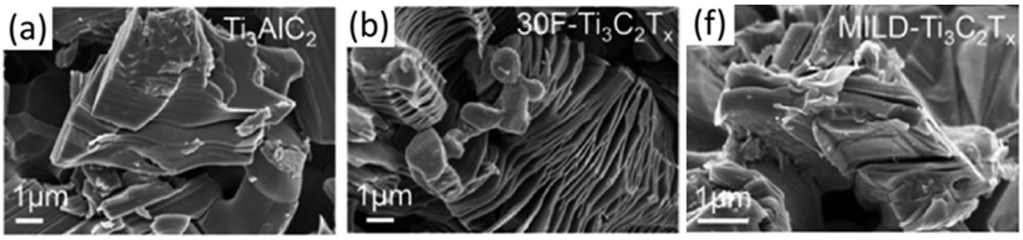

Figure 2. SEM images of (a) MAX phase, (b)MXene derived after etching with 30 wt.% HF, and (f) MXene after getting etched with HCl and LiF [30]

More than 150 types of MAX phases have been reported, and 40 different MXenes with distinct stoichiometries.[7-8] Hundreds of more different stoichiometric MXenes have been studied computationally, and countless more compositions are possible as solid solutions.[7,11] The number of MXene will only continue to rise because there is a wide range of elemental combinations that could be formed by placing different elements in the M and X sites.[7] And there is also the added variability through different stoichiometric ratios.[11] These different compositions and chemistries provide accessibility to a spectrum of properties that can be

incorporated to engineer diverse materials and devices for different applications. Moreover, the surface chemistry of MXene can be further tuned by applying variable synthesis routes, thus, controlling the type and the concentration of functional groups attached to the surface provide further opportunities to engineer Mxenes' characteristics.[10]

1.3 *Properties of MXene*

Graphene has been hailed as a "wonder material" and has captured the imagination of a vast community of researchers.[12] Researchers saw potential in graphene's properties and hoped to bring about a breakthrough by implementing graphene's exceptional characteristics into achieving ambitious real-world applications, from high-speed electronics to supercapacitors, solar cells, and smart screens.[12] Despite widespread popularity, various factors have hindered its usage in large-scale real-world applications. For instance, the poor solubility of graphene has made it difficult to process graphene and use it in composites with other materials.[13] Similarly, keeping graphene free of defects to maintain its usability is another challenge for the mass production of graphene.[12] Here, the discussion on graphene's current challenges and outlook has been included as a preamble to establish a meaningful platform to discuss the properties of MXene. Since there are many similarities between MXene and graphene in terms of structure and properties, graphene's more familial background can add perspective to understanding the properties of MXene more critically.

Interest in MXenes has also been steadily increasing in the past decade since its discovery in 2011. In 2017, Anasori et al. reported that about 20 different

stoichiometrically distinct MXenes had been synthesized.[14] In 2021, the number of stoichiometrically distinct MXene synthesized had increased to 40.[11] MXenes' rise to prominence can be credited to its unique combination of properties such as superb electrical conductivity, outstanding mechanical robustness, and hydrophilicity, among others.

1.3.1 MXene Properties - Electrical Conductivity

Of all the remarkable properties of MXene, its conductivity is its most distinguishing characteristic. Moreover, MXenes' conductivity is tunable and can be altered by changing MXenes' composition, stoichiometry, and surface termination groups.[11] Therefore, the conductivity of MXene can range from that of a semiconductor to a superconductor.[10] In 2019, Ronchi et al. reported that the conductivity of $Ti_3C_2T_x$ MXenes varied from 850 to 9880 $S.cm^{-1}$(Figure 3).[10] Whereas for Mo_2CT_x MXenes, the conductivity can be in the range of 3 $S.cm^{-1}$ to 250 $S.cm^{-1}$(Figure 3), depending on the treatment conditions. [10,17] Similarly, Urbankowski et al. have found the conductivity of V_2CT_x to be between 400 and 1500 $S.cm^{-1}$. [10,17] The conductivities of Mo_2NTx and V_2NT_x, on the other hand, were found to be around 2000 $S.cm^{-1}$ and 4000 $S.cm^{-1}$, respectively, when measured at room temperature.[17]

Likewise, Kamysbayev et al. showed how the conductivity of MXenes can be controlled by changing the terminal groups.[15] Etching MAX in HF usually results in MXene with termination groups such as -O, -OH, and - F. However, the synthesis of MXenes can be conducted in Lewis acidic molten salts to produce MXenes with other different terminal groups such as O, NH, S, Cl, Se, Br, and Te.[15] Kamysbayev et al. found that terminating Nb_2CT_n with Se increased the resistivity while terminating the MXene with Se decreased its resistivity. [15]

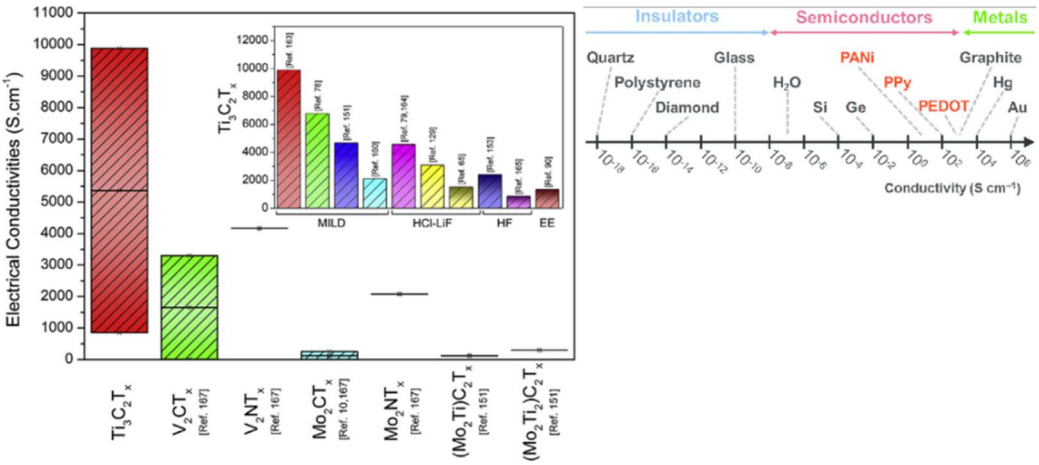

Figure 3. A bar graph (right)showing the range of electrical conductivity values of various MXenes reported in the literature, with a line graph showing the electrical conductivity range coupled with the material classification based on the conductivity [10,55]

The elemental composition, surface terminal groups, and stoichiometry clearly dictate the electrical properties of MXenes. However, the difference in conductivity in MXenes can also be caused due to the etching conditions. [10] For instance, MXene flakes produced under milder etching conditions with a lower concentration of HF and a shorter etching time were found to have superior electrical conductivity as the flakes consisted of fewer structural defects and resulted in larger lateral sizes. [18-19].

Earlier in 2014, when Naguib et al. formed free-standing thin discs by cold pressing MXene powders, they found the resistivity of the discs to be 22 Ω/sq for $Ti_3C_2T_x$ and 339 Ω/sq Ti_2CT_x.[16] These values were comparable to that of multilayer graphene, as Li et al. have reported that 4-layer graphene had a resistivity of 350 Ω/sq.[26] In the latest review published in 2021 by Naguib et al., the authors have mentioned that MXene ($Ti_3C_2T_x$) has been reported to possess conductivity of 24,000 S cm^{-1}, which was obtained by optimizing the etching process.[11] This value far surpasses any conductivity values of graphene and carbon nanotube samples reported in the literature. [10,20-22]

1.3.2 MXene Properties - Mechanical Property

Another property of interest is MXenes' mechanical property. Although MXene composites have primarily been studied for energy storage as capacitors and electrodes, they have increasingly been considered for other applications. [6] Researchers are considering MXene for applications such as biomedical devices, catalysis, water desalination, water purification, gas separation, and piezoresistive sensors, to name a few. [6, 23] For all these applications, MXene composites must be mechanically robust and endure continuous cycles of applied stress without failure. [23]

While there are numerous ways to characterize the mechanical properties of bulk material, there has not been much advancement in characterizing the strength of 2D materials. [23] Nevertheless, ever since Lee et al. used nanoindentation to measure Young's modulus for a monolayer graphene sheet via an atomic force microscope (AFM), it has become a standard technique to measure the mechanical properties of all 2D materials. [24] Likewise, when Lipatov et al. used this method to measure the

mechanical property of a single and bilayer $Ti_3C_2T_x$ MXenes, they found that the Youngs's modulus of single layer $Ti_3C_2T_x$ MXene was 0.33 ± 0.03 TPa (Figure 4).[13,30] This value is lower than Young's modulus of single-layer graphene, which is 1 TPa. However, this value is still higher than the values reported for Young's modulus of a monolayer graphene oxide (GO) which, according to Suk et al., is 207.6 GPa. [13,25,30] Although graphene is the strongest material known to date, processing graphene has been challenging due to its hydrophobicity.[13] On the other hand, GO is solution-processed oxidative exfoliation of graphite prepared in acid solutions, which is prevalently used in large-scale applications as an alternative to graphene.[13] Therefore, it is more suitable to compare MXene with GO than with graphene when it comes to mechanical applications. And so, MXenes ($Ti_3C_2T_x$) are the strongest of any solution-processed 2D material to date. [13]

In addition to experimental studies, computational studies have also been conducted to estimate the mechanical properties of MXene using density functional theory (DFT). In a similar study, Zhang et al. used DFT calculations to compare structure stability, surface chemistry, and electronic properties of different carbide and nitride MXenes with various 'n' layers. [27] They discovered that the structural stability of both carbide and nitride MXenes increased with the increasing 'n' layers.[27] However, in the case of elasticity, Young's moduli decreased for both the carbide and nitride MXenes with the increasing 'n' layer.[27] Zhang et al. also studied the effect of terminal groups on the structural stability of the MXenes and concluded that -O and -F formed more structurally stable MXenes than the -OH groups.[27]

In many instances, the experimental values are lower than the previously calculated computational estimations.[13, 23] This is because, for most of the computational calculations, pristine MXenes were used, and defects in MXene that usually occur due to the etching process were not considered while performing the calculations.[13,23] This further proves that just as for the electronic properties, the etching process also affects the mechanical properties of MXenes.

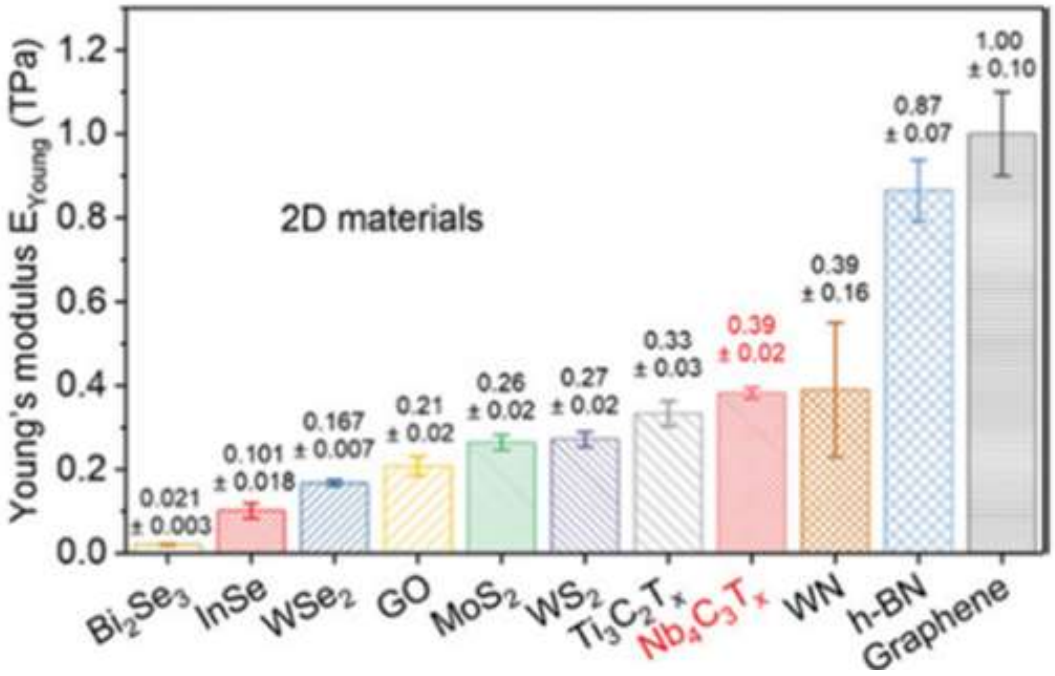

Figure 4. Bar showing the Young's modulus for various 2D materials

1.3.3 MXene Properties – Hydrophilicity

Another advantageous feature of MXene is its hydrophilicity. Etching of MAX phases removes the 'A' layer and places functional groups such as -OH, -O, and -F on the surface. The functional groups (-OH, -O, and -F) render the etched MXene flakes negatively charged at neutral pH.[29] The presence of charge on

MXenes' surface is responsible for producing a stable colloidal system over a wide range of pH. [29,30] Moreover, the hydrophilic nature of Mxenes enables them to have favorable interactions with multiple polymeric matrices to form stable composites. [10,11]

1.4 Application of Mxenes

The hydrophilicity of MXenes sets it apart from the other 2D materials, including graphene, and gives it an advantageous edge when it comes to processing and forming stable composites with other polymers for large-scale applications [10] Furthermore when this feature of MXenes is combined with excellent electrical conductivity and impressive mechanical strength, MXenes becomes a formidable choice to be used in multiple applications due to its versatility. MXenes have been primarily used in energy storage, but researchers have recognized their potential for other fields as well.[6] Some other applications of MXenes mentioned in the literature are catalysis, biomedical devices, environmental-related applications as absorbents for water remediation and desalination, and batteries. [35] Below are short discussions about some of the applications of MXene-derived material and composites to understand MXenes' role, behavior, and outlook for future applications and design.

Figure 5. Pie chart showing different application of MXenes [6]

1.4.1 Application of MXene - Flexible Battery

MXene hydrogels and aerogels are currently being considered for the construction of flexible batteries for wearable electronics. Porous structures of MXene-based aerogels are especially favorable because of their ample interior space, which can be used to load active material without sacrificing the aerogel's ionic or electronic properties.[35] Additionally, an abundance of oxygen functional groups in MXene-reduced graphene oxide (rGO) aerogel has been shown to assist in the uniform stripping of Li in the Li-metal battery system.[35] Besides, the 3D porous network provides an excellent conductive path to transport electrons across the battery.[35,36] And the MXene-rGO aerogel-based battery also demonstrated

remarkable stability when the stepwise capacity of the battery was increased from 1 mAh cm^{-2} to 5 mAh cm^{-2}. [35]

1.4.2 Application of MXenes - Biomedical applications

MXenes have shown potential to be used in cancer therapy and fabrication of biomaterial for tissue engineering owing to their biocompatibility and anti-microbial, anti-inflammatory, and immunomodulatory properties. [37] Besides, MXene-based hydrogels have also been studied for drug delivery of anti-cancer drugs. Hydrogel consisting of MXene ($Ti_3C_2T_x$) and nano-cellulose has successfully demonstrated controlled drug release of Doxorubicin by using MXenes' photothermal ability.[35] Moreover, hydrophilicity and the porous structure of the hydrogel facilitate the uniform and high loading of the drug.[35]

1.4.3 Application of MXenes - Sensing Applications

Researchers are trying to model the sensing system of robots/machines after the human nervous system to develop the next-generation intelligent machine. [38] When a human holds a fragile object without breaking it, the task is done by accurately perceiving the object's fragility and with a sensing memory that allows learning via repetitive trials. [38] MXene, $Ti_3C_2T_x$ has been studied to be used as sensors and in memristors (to store information on data performance) to develop a similar kind of sensing capability in a robotic system. [38] MXenes have been investigated in developing tactile sensors because of their excellent electrical conductivity and facile assembly into 2D films or 3D porous structures. The film/porous material's internal structure and morphology change instantaneously in response to external stimuli, thus

allowing for rapid measurement of stress. [38] And thus, they have a great potential to be used in human-machine interaction because of their ability to provide real-time measurement of physiological signals. [38]

1.5 *Piezoresistive sensors and the role of MXene aerogels*

There is a strong demand to develop an intelligent pressure sensing material for the next generation of machines and robots. These next-generation pressure sensors need to possess high sensitivity for different pressure ranges and superior mechanical durability. Different sensing scenarios require the sensors to bear correspondingly different characteristics. For instance, for wearable pressure sensors, the sensors must also be ultra-lightweight and flexible and simultaneously be mechanically robust and highly sensitive.[31,32] Pressure sensors designed to measure weak blood pressure signals from deep veins in a human body must have the capability to detect stress as low as < 0.001 Pa.[33] While soft robotic grippers will need sensors with sensitivity and detectability to operate in the range between10 kPa to 100 kPa.[34] The piezoresistive platform could be the most convenient and favorable means to construct a sensor for such complex applications because of its high sensitivity, making it suitable to operate in dynamic conditions.[31,40] Besides, a piezoresistive device permits a broad choice of active material that can be easily integrated into the device to suit the nature of the application.[31,33]

A material exhibits piezoresistive property when its resistivity changes in response to mechanical deformation. [40] Piezoresistive sensors have some prominent desirable traits such as simple fabrication, low energy consumption, easy signal readout, and a broad range of pressure detection. [31]

Conventionally, piezoresistive sensors have been bulk materials composed of elastomers filled with conductive fillers such as reduced GO (rGO), carbon nanotubes (CNT), metal particles, and conductive polymers.[31] However, the significant disadvantages of these sensors are their poor sensitivity and the inability to detect subtle forces.[31,40] One of the approaches discussed in the literature to increase the sensitivity of these piezoresistive sensors is to incorporate transistors to amplify the signals. [31] Another possible solution is to fabricate porous and hierarchical micro-structured material. [31,33] Usage of porous material might be a preferable approach. As the reported sensitivity of porous material has been high in literature, reaching up to >100 kPa and nanoscale porosity of the hierarchical porous structures can enable the detection of ultra-low forces. [33]

There have been multiple attempts to fabricate conductive aerogel using 2D nanomaterials such as graphene oxide, carbon nanotubes, and MXene. [33] MXene aerogel has a competitive edge over other 2D materials because of its superior electrical conductivity, exceptional mechanical property, and hydrophilicity.

While it is true that individual MXene monolayered nanosheets have displayed exemplary strength when measured via AFM nanoindentation, constructing “MXene-only” aerogel with sufficient mechanical robustness has been challenging. [13,40] This is because MXene nanosheets form discontinuous macrostructures due to their low aspect ratio. [40] Nonetheless, composites consisting of MXene with other co-building blocks have produced aerogels with improved mechanical strength. [40] Likewise, the

following section will present a detailed literature review on some of the valuable work done by other scientists and researchers to study and construct MXene-based aerogels.

1.6 Literature Reviews

1.6.1 Literature review #1 – "Wood-inspired superelastic MXene aerogels with superior photothermal conversion and durable superhydrophobicity for clean-up of super-viscous crude oil" [56]

Seeing how wood could efficiently transport water through its xylem via capillary action, Cai et al. wanted to incorporate a similar strategy to efficiently absorb high-viscous crude oil from water. In addition, Cai et al. also sought to make the material superhydrophobic, mechanically robust, and have a superior solar-to-heat conversion with ultra-light density. They chose MXene-based aerogels to develop such material because of its good thermal conductivity and excellent solar-to-heat conversion. Besides, the microstructure of the MXene aerogels can be easily tuned by controlling the fabrication method.

In this study, Cai et al. fabricated the aerogel by first mixing 0.4 wt.% of functionalized nano-cellulose crystal(f-NCC) suspension with 0.5 wt.% of MXene suspension. The mixture was stirred for 2 hours, followed by the addition of 2 g of waterborne polyurethane (WPU). After that, the mixture was stirred for 6 hours. Then, the complex suspension was poured into a circular tube and frozen using liquid nitrogen via directional freezing. After that, the frozen complex suspension was freeze-dried for two days at -60 ºC. The solid content of the complex suspension was 5 wt.%

The resulting aerogel, as shown in Figure 6, exhibited anisotropic characteristics. The aerogel formed aligned lamellar microchannels in the longitudinal direction, while at the cross-section, the aerogel had a cellular honeycomb structure. The size of the cells was ~ 100 µm.

Figure 6. SEM images of the MXene aerogels (a) and (b) are cross-section images. (c) is the image of longitudinal section

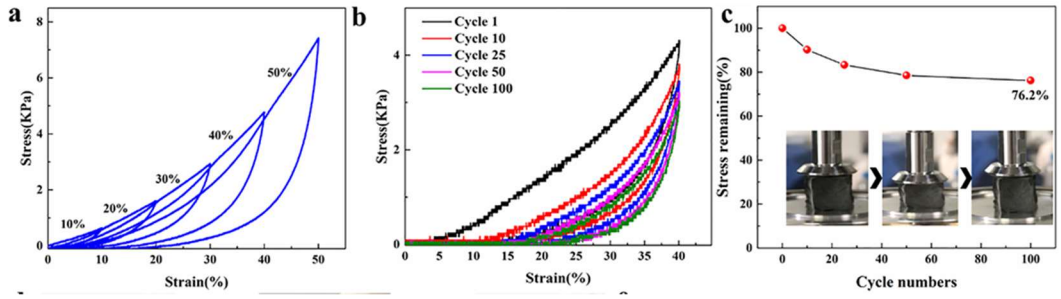

Figure 7. (a) stress-strain profile as the strain increased from 10% to 50%. (b) stress-strain profile of the MXene aerogel at 40 % strain for various cumulative fatigue cycles. (c) stress retention of the aerogel as a function of the number of increasing fatigue test cycles

The MXene aerogel was tested for its mechanical robustness and elasticity via multiple compressive test cycles. The stress-strain profile of the MXene aerogel rapidly steepened as a response to the increasing strain from 10 to 50%, reaching the maximum stress at 6.5 kPa at 50% strain (Figure 7a). Additionally, the aerogel was put through 100 compressive fatigue test cycles to test its durability. In the end of 100 cycles, the MXene aerogel was able to display superb elasticity by retaining 76.2% of the initial maximum stress.

1.6.2 Literature review #2 - "Highly Compressible, Thermally Stable, Light-Weight, and Robust Aramid Nanofibers/Ti3AlC2 MXene Composite Aerogel for Sensitive Pressure Sensor" [42]

The authors aimed to develop a piezoresistive pressure sensor with a wide range of detection limits and high sensitivity in this study. Here Wang et al. used aramid nanofiber (ANF) and MXene ($Ti_3C_2T_x$) to form ANF/MXene composite aerogel via vacuum filtration followed by freeze-drying.

Wang et al. used 30 wt.% CNF suspension with increasing wt.% of MXene suspension to construct porous composite aerogels. Four different recipes were used with varying compositions and one pure ANF aerogel for reference. They observed a downward trend in strength with increasing MXene content (Figure 8). In conclusion, the authors found 30 wt.% MXene/ANFs, which had an equal ratio of CNF and MXene, to be the best performing aerogel with simultaneously satisfying mechanical and electronic properties. The aerogel could reach up to 36 kPa compressive strength at 30% strain with a sensitive sensing property of 128 kPa^{-1} and the lowest detection limit of 100 Pa.

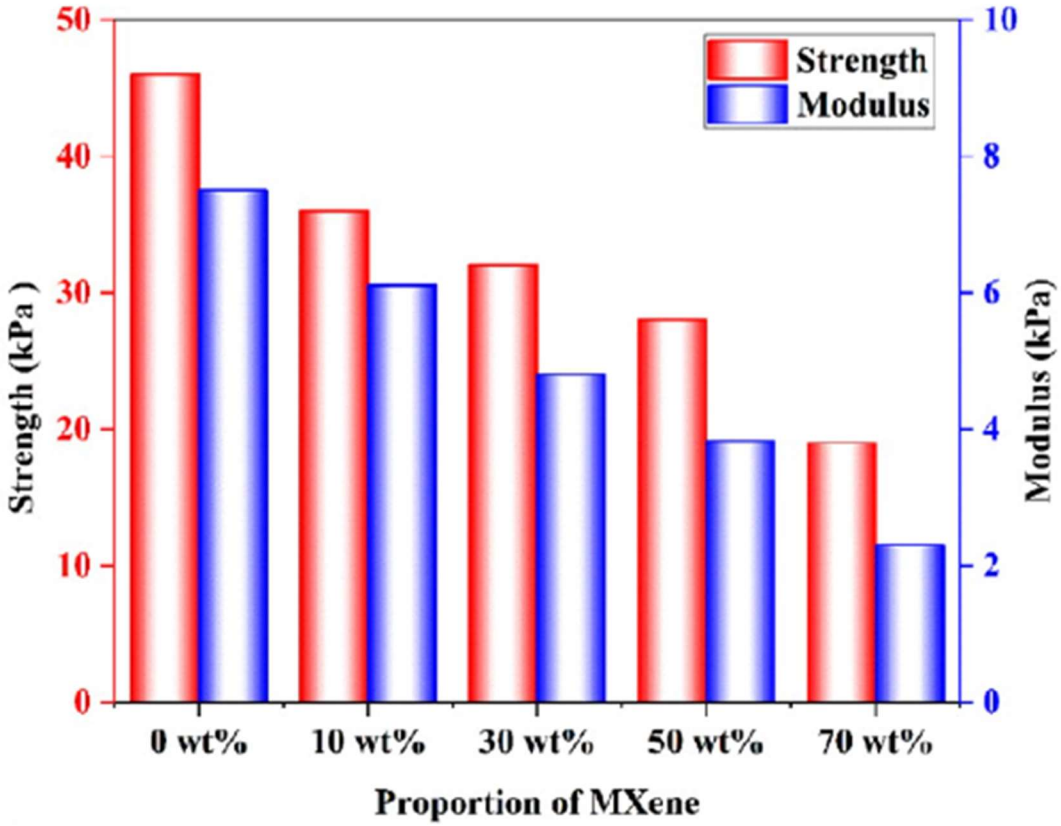

Figure 8. A bar graph showing strength(at 30% strain) and Young's Modulus of MXene aerogels with increasing MXene ratio

Chapter 2: Fabrication of MXene Aerogels via automated pipetting system

2.1 MXene Aerogel - The Building Blocks

Four building blocks are used in this study to fabricate MXene aerogels. These four building blocks are – MXene ($Ti_3C_2T_x$), cellulose nanofiber (CNF), gelatin, and glutaraldehyde. The primary goal of this study is to investigate the influence of each building block and the fabrication recipe via active learning and eventually design the mechanical properties for an aerogel through the recipe suggested by the machine learning model.

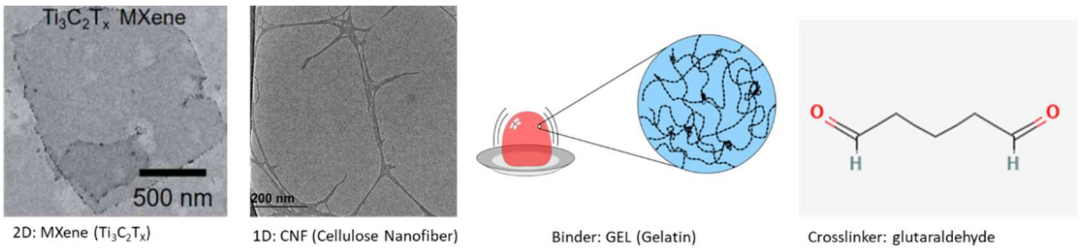

Figure 9. Four building blocks used in the preparation of MXene Aerogels [50-52]

MXene is the core component of the aerogels that endows them with electrical conductivity, which is integral to the piezoresistive property of the aerogel.

MXene also contributes toward providing mechanical strength to the material when combined with other composites. There are ample examples in the literature that show how "MXene-only" aerogels form discontinuous structures, resulting in failure for various targeted sensing applications. [40,44] Moreover, the literature reviews in the previous section (1.6.1-1.6.2) demonstrate how combining MXene with other polymers

such as CNF and ANF has a synergistic effect in improving the mechanical properties of the aerogel.

CNF was chosen as one of the building blocks because multiple accounts in the literature have reported that CNF imparts good mechanical strength and flexibility to the aerogels. [40,41,43,44] Furthermore, CNF owing to its 1D structure, high aspect ratio, and negatively charged terminating groups, produces a stable colloidal system, and helps in effectively dispersing monolayer MXenes. [43, 44] As the gelation occurs, CNF acts as a "nano-mortar" and binds MXenes into a nacre-like high-strength structure, and forms honeycomb cellular architecture at the micro-level just as shown in Figure 6 and 13. [44] This phenomenon creates inter-layer spacing between the MXene layers, which is instrumental in providing hierarchical piezoresistive property to the aerogel. [43] Additionally, CNF is lightweight, inexpensive, renewable, and easily degradable, making it an attractive component for the aerogel from the future scale-up, environmental and sustainability point-of-view [43]

CNF/ Gelatin is one of the well-explored systems for constructing hydrogels and aerogels. For instance, as CNF and gelatin both are natural polymers, CNF/Gelatin has been studied extensively to develop hydrogels for biomedical applications. [45] In their review, Jiang et al. reported that the highest breaking strength demonstrated by a CNF and gelatin hydrogel was 249.37 kPa which is 5.75-fold higher than the strength of pure gelatin hydrogel. [45] The increase in strength results from the favorable interactions between the hydroxyl groups on CNF and the carboxyl and amino groups of gelatins which binds the long chains of CNF with gelatin to form a complex triple helix.[45]

Lastly, glutaraldehyde is the fourth building block, and it has been used in this study as a cross-linker in the fabrication process to strengthen the aerogels further. Glutaraldehyde is a prevalent means to cross-link the biopolymers with hydroxyl groups. [47] They have been widely used with gelatin because of their strong affinity towards gelatin's anime groups. [47]

2.2 Synthesis of single-layered MXene suspension

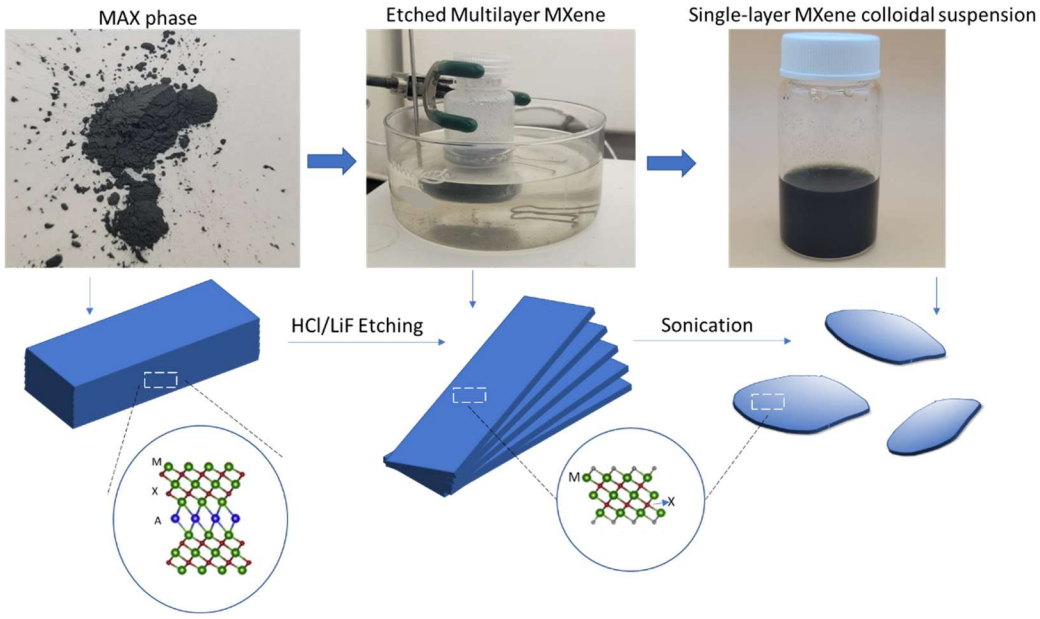

Figure 10. Schematic showing the synthesis of MXene from the MAX phase to exfoliated MXenes. Molecular structure of MAX and MXene extracted form Ref. [10]

2.2.1 MXene suspension – Materials

Lithium fluoride (LiF, powder, <100 μm, ≥99.98% trace metals basis) and hydrochloric acid (HCl, 37%) were purchased from Sigma-Aldrich.

2.2.2 MXene Suspension – Synthesis

In this study, the Ti_3AlC_2 precursor MAX phase was used to synthesize a suspension of 2D single-layered $Ti_3C_2T_x$ MXene nanoflakes just as portrayed in Figure 10. First, 40 ml of 9 M HCl solution was heated in a plastic bottle at 35 ºC. 3 g of LiF was added and dissolved in the HCl solution when the temperature stabilized. After that, MAX precursor was added slowly so as not to cause any sudden change in the temperature. Then, the mixture was kept stirring for 24 hours at 35 ºC to etch away the Al layer from the MAX phase.

The reaction products were washed and centrifuged with 2 M HCl for the first three times. The following washes were carried out with DI water until the pH of the suspension was ~ 5-6. After that, the supernatant MXene suspension was collected and sonicated in a cold-water bath for 60 minutes. Then, the MXene suspension was centrifuged at 3000 rpm for 30 minutes, and the resulting suspension was collected as the end product.

2.3 Tempo Oxidation of CNF suspension

2.3.1 Tempo oxidation of CNF – Materials

Kraft bleached softwood pulp, 2,2,6,6-Tetramethylpiperidine 1-oxyl radical (Tempo 98%), sodium bromide (NaBr, >99.0%), sodium hypochlorite(NaClO), sodium hydroxide (NaOH), sodium carbonate (Na_2CO_3), and sodium bicarbonate ($NaHCO_3$) were purchased from Sigma-Aldrich

2.3.2 Tempo oxidation of CNF – Synthesis

First, 250 ml of 0.1 M of buffer solution was prepared. 2.12 g of Na_2CO_3 was mixed in 200 ml of DI water. Simultaneously, 0.42 g of $NaHCO_3$ was mixed in 50 ml of DI water. Then, both the solutions were combined to prepare the buffer solution in the ratio of 4:1 of Na_2CO_3: $NaHCO_3$.

TEMPO solution was prepared by dissolving 78.125 mg of TEMPO in 25 ml of the buffer solution. Then, sodium bromide solution was made by dissolving 514.45 mg in 50 ml of the buffer solution.

After that, 34.535 g of wet pulp was mixed with the TEMPO and sodium bromide solutions. Then, 115 g of buffer solution was added, and the mixture was blended using a food processor at 7000 rpm. After 35 ml of NaClO was added dropwise to the pulp suspension while the suspension was kept stirring at a medium speed. The pH was controlled at 10.5 by monitoring and adding 3 M NaOH solution when the pH dropped below 10.5. The reaction mixture was kept stirring for 2 hours while maintaining the pH at 10.5.

After the reaction, the tempo-oxidized fibers were washed via Buchner filtration. The residual tempo-oxidized fibers were then re-dispersed in 500 ml of DI water by stirring the mixture at 700 rpm for 30 minutes. The washing process was repeated two more times to get rid of the reactive agents thoroughly.

The resulting CNF suspension was collected and stored in a separate container.

2.4 Preparation of gelatin solution

2.4.1 Preparation of gelatin solution – Materials

Gelatin from porcine skin (powder, gel strength ~300 g Bloom, Type A) was purchased from Sigma-Aldrich.

2.4.2 Preparation of gelatin solution – Synthesis

To prepare 1 wt.% gelatin solution, 1 g of gelatin was added in 100 ml water and kept stirring at medium speed at 40 ºC until the gelatin dissolved.

2.5 Preparation of MXene aerogels via automated pipetting

2.5.1 Preparation of MXene aerogels – Material

1 wt. % suspension of CNF, MXene and gelatin were synthesized following the methods discussed in the section (2.1.1,2.2.1 and 2.3.1)

Silicone molds were purchased from Amazon.

2.5.2 Preparation of MXene aerogels – Equipment

OT-2 pipetting robot (Opetrons, USA) was used to assemble MXene, CNF and gelatin suspensions via automation to formulate the complex suspensions for MXene aerogel fabrication.

A lyophilizer was used to freeze dry the samples by sublimating water from the complex suspension system to form the porous aerogel structures

2.5.3 Preparation of MXene aerogels – Synthesis

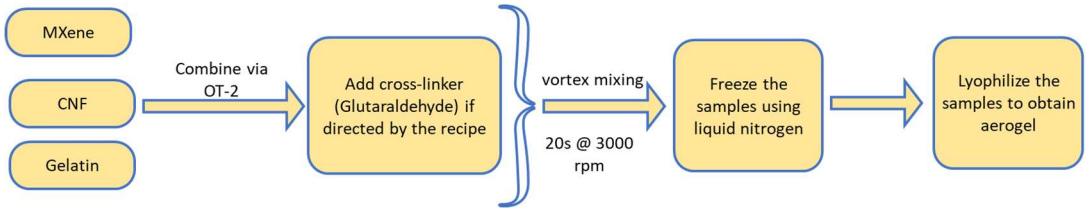

Figure 11. Process flow diagram depicting the fabrication of MXene aerogel

As illustrated in the process flow diagram in Figure 11, first, a batch of 1 wt. % mother solutions of MXene, CNF, and gelatin were prepared. After a protocol file containing the instructions to prepare the aerogels of varying recipes was uploaded to the OT-2 system, the mother solutions were placed inside the OT-2 (shown in Figure 12) to assemble a batch of multiple complex suspensions.

The complex mixtures were prepared in 15 ml centrifuge tubes. Cross-linker (glutaraldehyde) was added to the suspension if the recipe required it. Then, the complex formulations were vortex-mixed for 20 seconds at 3000 rpm. After that, the suspensions were poured into a silicone mold and were refrigerated overnight. The next day, the complex suspensions were frozen in liquid nitrogen and were freeze-dried for a week at – 80 ºC. MXene aerogels were finally obtained after the drying process.

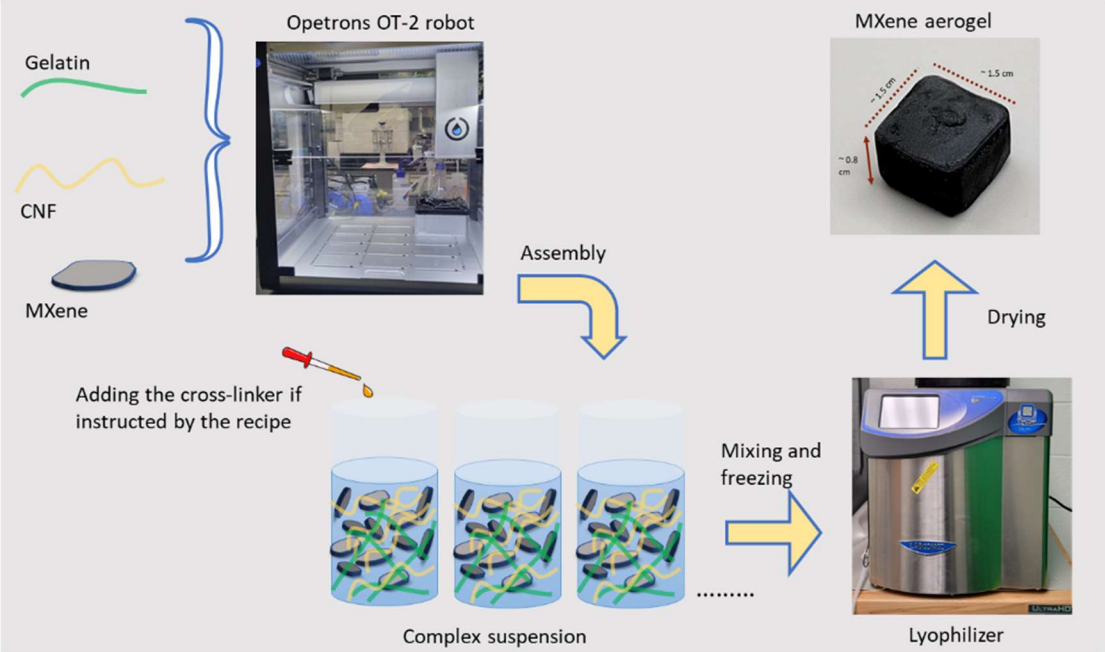

Figure 12. Schematic illustration of fabrication of MXene aerogel

Chapter 3: Engineering a novel approach to custom design mechanical properties for piezoresistive aerogels by understanding the current challenges

3.1 Research Incentive

This study aims to discover the underlying design principles of the MXene-based piezoresistive sensors so that they can be applied to rapidly design sensors for diverse mechanical (compressive) conditions. Depending on the nature of the application, the chemical, physical and electrical properties of the sensing device are altered to tune the device's performance. Many studies have investigated this problem in the context of MXene-based aerogels to produce designs for piezoresistive sensors for next-generation machines. However, to date, we still lack a clear and comprehensive understanding of the correlation between chemistry, structure, properties, and performance of such aerogels. Therefore, before setting out to do our own investigation to reach the agenda of this study, it is important to recognize and critically assess some of the current work done in this field. It is imperative to identify and address the limitations and restrictions that are commonly found and likewise make improvements to address those challenges to make any headway in the field of MXene-based piezoresistive aerogels.

3.2 A critical assessment of a current study highlighting the use of conventional approach

3.2.1 Literature review #3 – "Super-elastic and ultralight electro spun carbon nanofiber/MXene hybrid aerogels with anisotropic microchannels for pressure sensing and energy storage" [41]

The authors fabricated (CNF) Carbon Nanofiber/MXene ($Ti_3C_2T_x$) hybrid aerogel with an ultra-low density of 4.87 gm/cm^3. Qin et al. constructed the aerogel by first freezing the suspension consisting of MXene and CNF using liquid nitrogen and subsequently freeze-drying it.

The resulting composite was an anisotropic porous structure with laminar channels and cellular architecture (Figure 13).

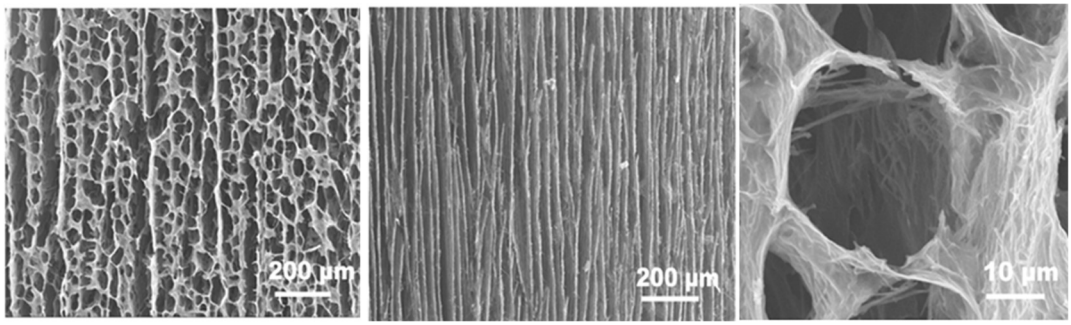

Figure 13. Showing microstructure of the MXene aerogel from the top, side and magnified view

The authors synthesized five aerogels composed of five different recipes, two of which were "MXene-only" and "CNF-only" aerogels used as reference.

CNF/MX-1, CNF/MX-2, and CNF/MX-3 had a mass ratio of CNF: MXene as 1:1, 2:1, and 3:1, respectively.

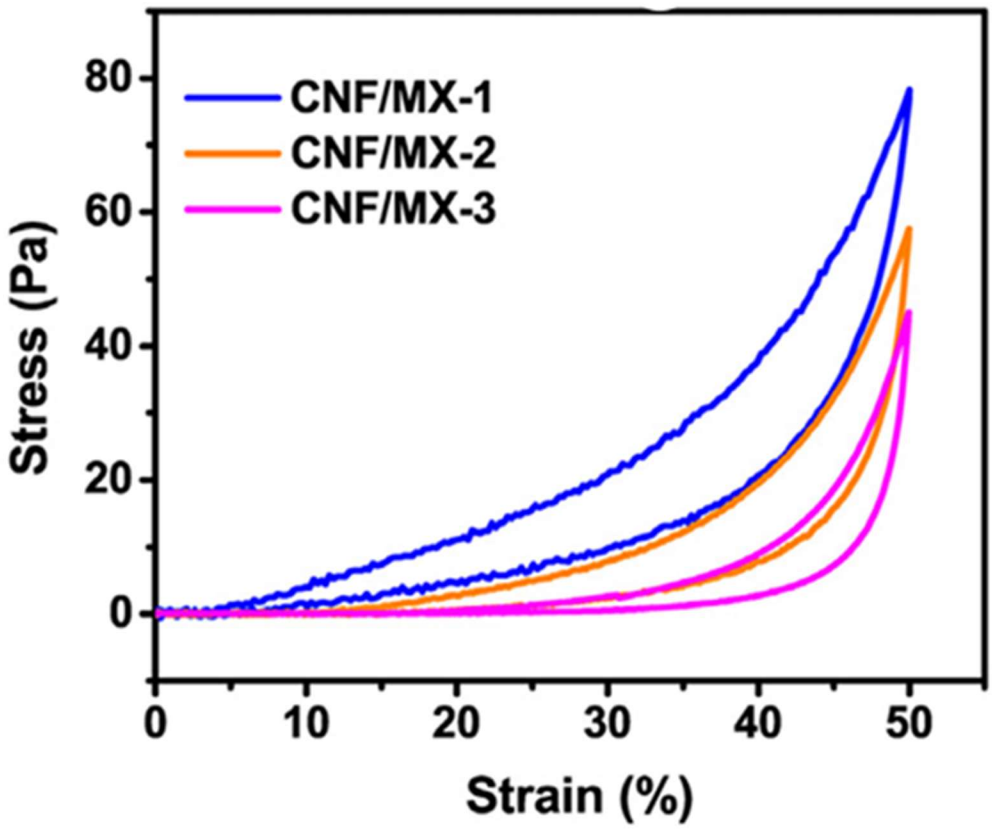

Figure 14. Showing stress-strain curve of MXene aerogel samples after 500 compression cycle

The authors found that "CNF/MX-1" aerogel consisting of a 1:1 ratio of MXene and CNF with mass loading of 0.7 wt.% was able to perform the best out of the three recipes tested in the experiment, exhibiting 96.4% stress retention after 500 compression cycles (Figure 14). When the aerogel was further tested for its pressure sensing properties, the authors found that the detection limit of the aerogel was (<5 Pa), while the sensitivity of the sensor was 65 kPa^{-1}.

3.2.2 Literature Review - Summary and discussion

Although Qin et al. were able to demonstrate MXene aerogel with sound mechanical and sensing properties, they did not give an explicit explanation about what aspect of design or composition of the aerogel contributed to such properties. Based on the data presented in the paper by Qin et al., the mechanical strength of the aerogels decreased with the increasing mass fraction of CNF. Firstly, three data points are not enough to uncover the full expanse of influence that CNF can have on the aerogel's performance. Secondly, the authors did not discuss how and why increasing CNF content resulted in the low mechanical strength in the aerogels.

Even though this study provides a good reference point for understanding some design aspects of MXene aerogels, an integral piece of information that elucidates the effect of composition and chemistry of the building block on the mechanical performance of the aerogels is missing.

For instance, through this study, it can be inferred that increasing the CNF content will prove unfavorable in optimizing the mechanical strength of the aerogels. However, in another study (section1.6.2), it was concluded that in an aerogel system consisting of ANF and MXene, increasing the MXene ratio caused lower mechanical strength. Therefore, most studies have optimized the aerogel properties for a given application through many rounds of trial-and-error, thus, lacking a thorough comprehension of the relation between the role of building block and microstructure, morphology, and properties of the MXene aerogels

3.3 Inherent challenges found in the current approach to engineer for mechanical properties of piezoresistive aerogels

Many factors influence the performance of MXene aerogel-based piezoresistive sensors, from the selection of the material to the device's design. Additionally, the morphology of the porous material, stiffness of the material, and the aerogel's conductivity and sensitivity also dictate the characteristics and performance of the sensor. These properties, in turn, are controlled by the composition of the composite aerogel material, fabrication technique, and solid content present in the aerogel system. These factors can behave independently to cause changes in the properties of the aerogel. At the same time, these factors can also display more complex behavior, such as having a synergistic effect when coupled with other factors. In any case, after reviewing current literature, it can be deduced that gaining a comprehensive knowledge of the underlying design principles of MXene aerogel-based piezoresistive via the conventional trial-and-error is virtually impossible because of certain inherent flaws and challenges found in the approach, which are listed below-

- The conventional approach, which uses a trial-and-error methodology, is time-consuming as it requires a case-by-case examination of each experimental scenario.
- The process becomes increasingly laborious and costly with the increasing degrees of freedom (DOFs)
- With a low data acquisition rate, human bias can affect the accurate representation of the extent of influence of the design parameters

3.4 Literature review #4 - an alternative approach that uses machine learning as to navigate complex design space consisting of multiple degrees of freedom "Automatic strain sensor design via active learning and data augmentation for soft machines" [53]

The authors of this paper proposed a novel approach to making custom-designed strain sensors. Yang et al. sought to develop strain sensors for any given strain condition to be applied in soft machines. As soft machines' motions are dynamic and complex, they require multiple sensors with distinct working capabilities. Therefore, the authors desired to develop sensors with an adjustable design property, so they could rapidly program the sensor's design to display customizable characteristics. Herein, Yang et al. used machine learning to build a prediction model which can be used to produce automatic designs for the strain sensors. The model was built to function in both directions – to give accurate performance predictions for a given fabrication recipe and to recommend fabrication recipes for specific performance.

Yang et al. fabricated the strain sensor by depositing a composite layer of single walled carbon nanotubes (SWNTs), $Ti_3C_2T_x$ -MXene and polyvinyl alcohol (PVA) on polyvinylidene fluoride (PVDF) membrane via vacuum filtration. When the resulting composite layer, identified as ps-MXene layer, was detached from the PVDF membrane by immersing in an ethanol bath, it formed a free-standing and planar ps-MXene layer (Figure. 15). The sensing characteristics of the strain sensor were engineered by deforming ps-MXene into various morphologies which consisted of combinations of periodic wrinkles and isotropic crumples as shown in Figure 15.

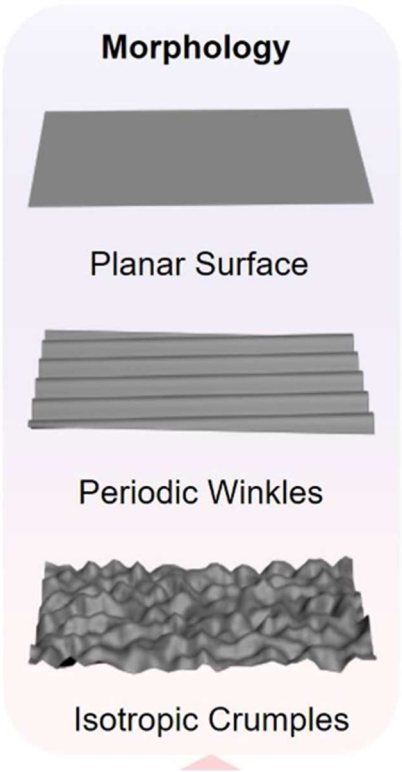

Figure 15. Strain sensor with various surface morphologies

The machine learning process used a three-stage framework which included boundary definition, active learning, and data augmentation.

3.4.1 Machine learning framework – 1st stage for robotic assistance

In the first stage of machine learning, the boundary of the feasible design space was determined. The overall design space for the strain sensors spanned in the region confined by PVA loading (wt. %) and SWNT loading (wt. %) ranging from 0 % to 100%, as shown in Figure 11, which covers all the possible compositions that could be used to fabricate the strain sensors. Three hundred fifty-one ps-MXene membranes were fabricated, consisting of varying MXene/SWNT/PVA mixtures with compositions that were evenly spread out over the entire design space. The detachment of these samples from the PVDF membrane was used as the determining factor to

define the boundary of the feasible design space. Based on the nature of the detachment, the samples were graded into three categories

- (1) Complete detachment indicating feasible cases
- (2) Detachment with visible fractures indicating fragile cases
- (3) No detachment indicating failed cases

The compositions of all the 351 ps-MXene layer samples and their detachment grades were then used as input data to train a support vector machine (SVM) classifier. The SVM classifier then produced a heat map outlining regions of various detachment possibilities (Figure. 16). The feasible design space was determined based on the heat map and was used in the second stage – active learning, to train the machine learning model to predict the recipes with high detaching possibilities.

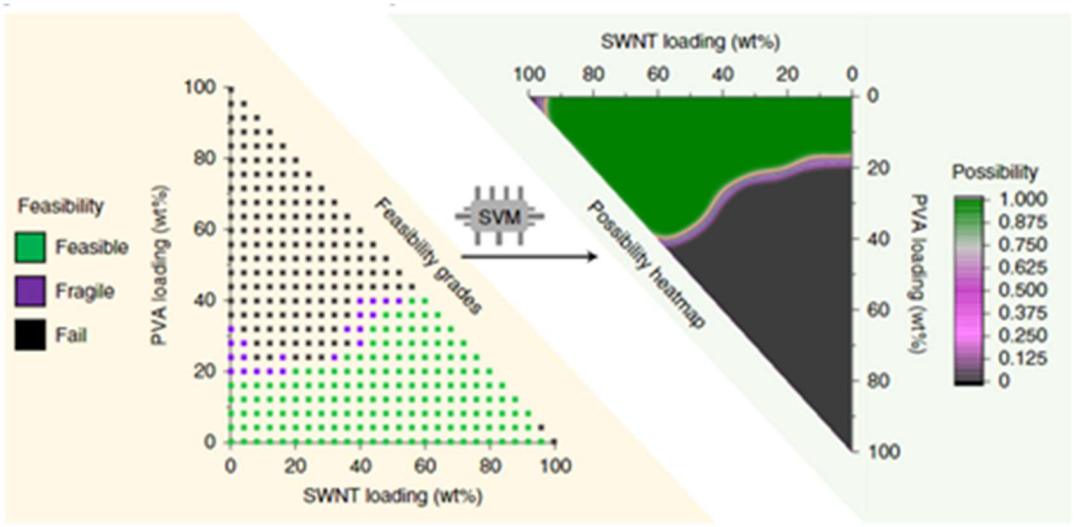

Figure 16. Showing training of the SVM classifier to produce a heat map outlining regions of various detachment possibilities

3.4.2 Machine learning framework – 2nd stage learning framework

After outlining the feasible design space, the space was utilized to further generate multi-degree of freedom design space by including two additional parameters – morphology and thickness. Multiple loops of active learning were executed to explore within this multi-degree of freedom design space to collect the representative data points and build the machine learning model (also called as navigation model). Each data point could be defined by its recipe which consists of four labels (SWNT loading, PVA loading, morphology, and thickness), and the sensor characteristic of the resulting strain sensor, which was also composed of four labels (ε_0, ε_{10}, ε_{100}, ε_{max}).

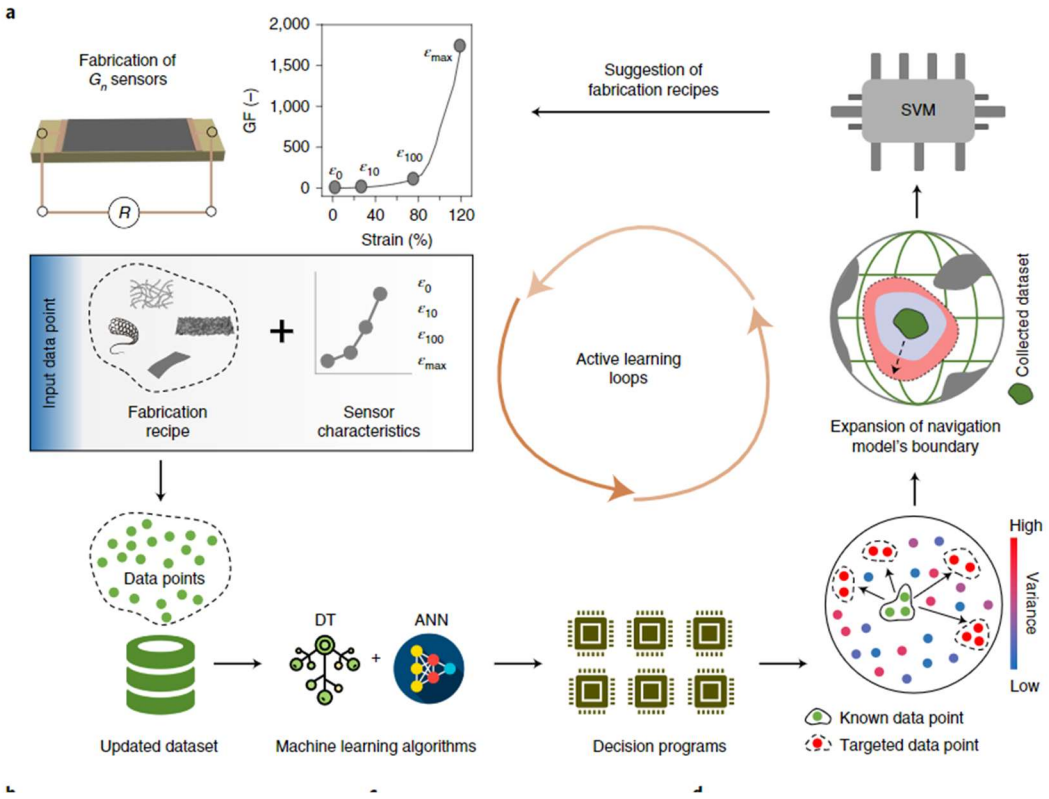

Figure 17 Showing schematic illustration of construction of a navigation model through active learning loop

The active learning loops were initiated by randomly choosing a dataset of 11 recipes. In the subsequent rounds of the active learning stage, as shown in Figure. 17, the model navigated through the design space by measuring the degree of space exploration and the prediction accuracy of the sensor performance. The boundaries of the navigation model changed with each advancing loop. The active learning concluded once the $\bar{L}$ representing the distribution of the data points and the mean squared error (MSE) of the prediction values stabilized.

3.4.3 Machine learning framework – 3rd stage

The model was further optimized by using virtual data points via data augmentation and genetic algorithm selection. Around 10,000 more data points were used to develop the model. The lowest mean relative error (MRE) of 24% was achieved after this optimization process.

3.4.4 Conclusion

A two-way model was developed after the completion of machine learning. This machine learning model was used to retrieve fabrication designs for various soft machine applications. For instance, a strain sensor was needed for a soft pneumatic gripper with design specification that the gauge factor (GF) [GF = $= \frac{(R-R_0)/R_0}{\varepsilon}$] was >100 within a strain range of 19-28%.

The model suggested a fabrication recipe with MXene/SWNT/PVA ratio of 53/45/2, the layer thickness of 942 nm, and morphology with periodic wrinkles. Here, Figure. 13 shows the GF- strain profile of the strain sensor fabricated using the suggested recipe. The figure shows how the strain sensor performed as per the design

request. Moreover, Figure. 14 shows a successful demonstration of the strain sensor where it was able to capture the gripping actions of two different objects with two distinct strain profiles showcasing strong sensitivity.

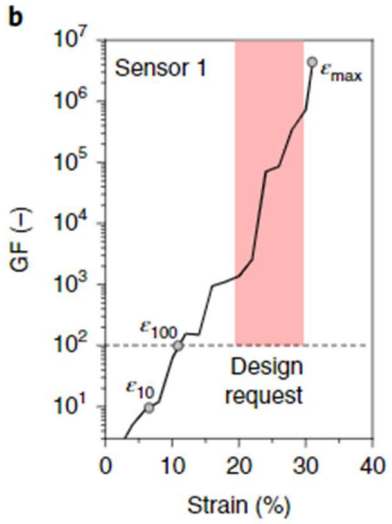

Figure 18. showing GF-strain profile of the strain sensor formed via the suggested recipe

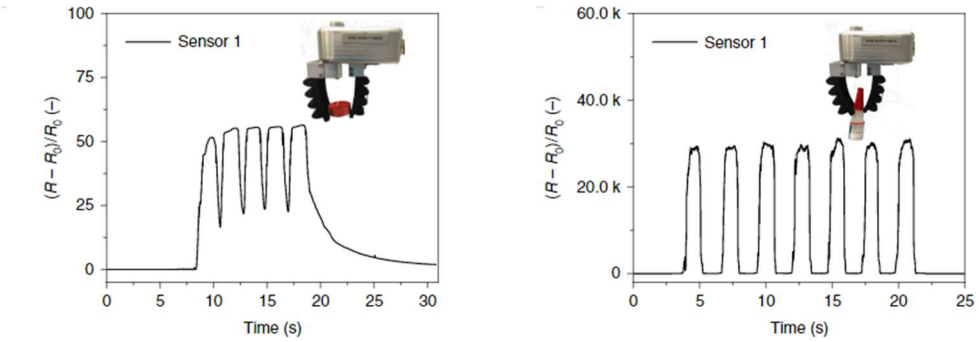

Figure 19. Resistance-strain profile of the suggested strain sensor while grasping a candle(right) and a glue (left)

3.5 Proposed plan of study

After being inspired by the approach used in the study described in section 3.4, a similar hybrid approach is undertaken to build a two-way machine learning (ML) model for the fabrication of MXene aerogels for piezoresistive sensors. Wet-lab experiments are conducted to synthesize and quality control the building blocks (MXene, CNF, and Gelatin), fabricate the MXene aerogels and measure the mechanical characteristics of the aerogels.

For this study to custom design mechanical properties in the MXene aerogel, the navigation model will have to explore a design space consisting of four degrees of freedom (DOF) which are-

- Composition (2 DOF: MXene, CNF, Gelatin)
- Mass loading (1 DOF: Concentration)
- Cross-linker (1 DOF: Glutaraldehyde)

The goal of this study is to use machine learning to build prediction models from the data generated in the wet-lab experiment. The ML model will function as a two-way model by suggesting the fabrication recipes for a given mechanical (compressive) property and estimating the mechanical property of the MXene aerogel for a given recipe, just as illustrated in Figure 20.

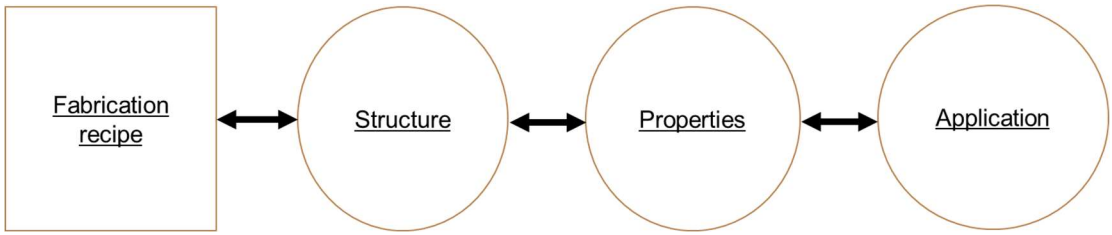

Figure 20. illustration of the governing hierarchical relation between the fabrication recipe, structure, properties, and application of the MXene aerogel

Chapter 4: Applying machine learning to develop piezoresistive sensors for various compressive mechanical conditions

4.1 Introduction

Machine learning is a powerful and versatile tool that operates using a data-rich system to construct models to make predictions and recommendations based on the observed underlying data trends and complex correlations. [53] One advantage of using machine learning is that in-depth knowledge of the subject matter is not required to build the models and draw valuable insights into the system.[54] Since the machine learning process is entirely data-driven, it eliminates preconceived biases which can introduce flaws in analyzing data, especially as the system becomes more convoluted at a multi-dimensional level. [54]

Due to its vast computational, machine learning has gained popularity in the field of material science as well. Machine learning has already been used to research catalyst design, drug discovery, and quantum dot synthesis. [54]

4.1.1 Necessity for robotic assistance

One challenging side of machine learning is that it requires a data-rich system to build sufficiently accurate prediction models. Ample data points need to be acquired to properly explore the design space to capture the correct characteristics of the system. For instance, when Yang et al. used machine learning to construct a model to generate automatic designs for the strain sensors, they collected 125 data points to conduct 12 active learning loops. [53]

Preparing MXene aerogels is a time-consuming and laborious task. Due to the high failure rates of the samples in the freeze-drying process, a larger batch of MXene aerogel needs to be prepared with multiple duplicates of the same aerogel sample. The preparation time of a single batch can take from several days to weeks, depending on the speed of preparation and the failure rate of the samples in the drying process. And so, this study realizes the necessity of automated systems to expedite the experimental efforts. Therefore, a collaborative approach is undertaken to conduct the experiments by employing robotic assistance such as OT-2 pipetting robot and UR5e robot arm. This collaborative approach has resulted in rapid data acquisition, and smooth coordination with the machine learning side.

4.1.2 Robot collaboration using OT-2

The OT-2 lab robot from Opetrons is an open-source automated pipetting system. The OT-2 robotic system was used to assemble the complex suspension (containing MXene, CNF, and Gelatin) to fabricate the MXene aerogels. A batch of MXene aerogel suspension which consisted of 66 samples was prepared in nearly three hours using OT-2. Thus, the preparation time of the suspension was ~3 minutes per sample.

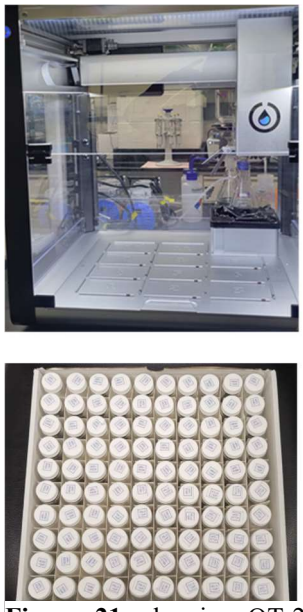

Figure 21. showing OT-2 robotic pipetting system (top) and two batches of samples prepared in 4 hours

4.1.3 Robot collaboration using UR5e

UR5e is a versatile collaborative robotic tool that have been applied to automate several industrial processes. It has been used for performing tasks such as machine tending, material handling and material removal.

The UR5e arm is used in this study to assist with compressive mechanical test of the aerogel samples. For the test shown in Figure 22, fifteen aerogel samples were tested in period of ~1 hour. UR5e robotic arm was programmed carry the aerogel samples from the stage set up (indicated by the orange arrow) to move to the bottom compressive plate of the Instron tensile tester (pointed by the yellow arrow in the figure). For this particular test, shown in Figure 22, the arm was also programmed to carry the samples in the photo-box to take a picture to measure the area of the samples.

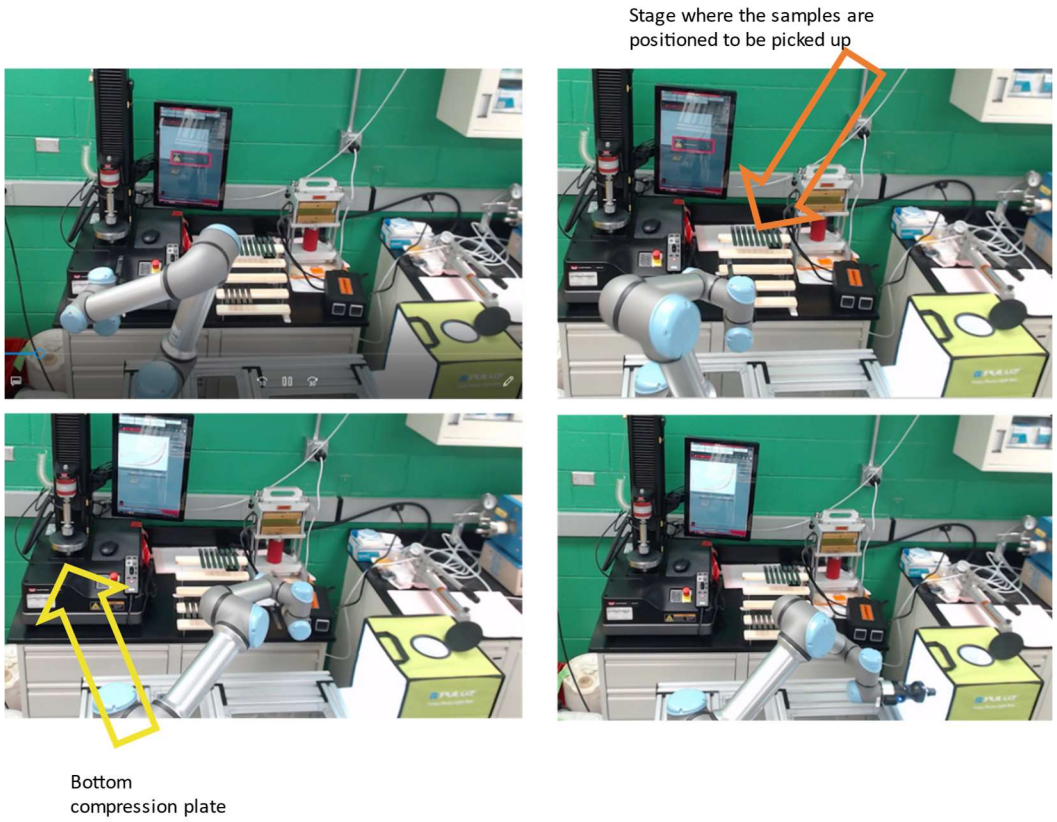

Figure 22. showing different portrays of the UR5e robotic arm as it conducted the compressive mechanical tests on the MXene aerogels

Machine learning applied in this study has a three-stage framework which includes (1) boundary definition as the first stage followed by (2) active learning and (3) data augmentation as portrayed in Figure 23

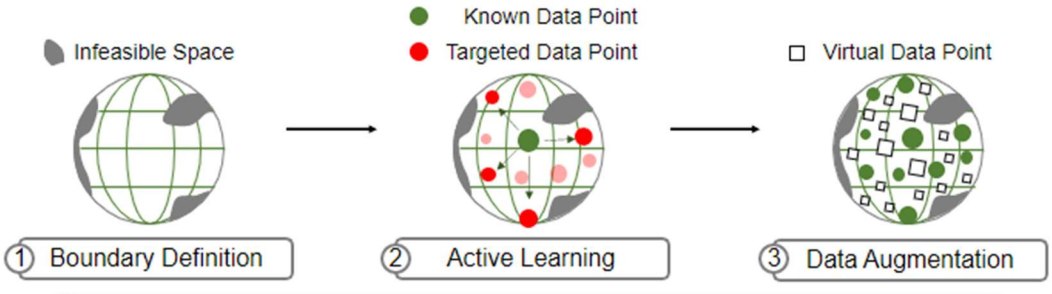

Figure 23. showing three-stage machine learning framework

4.2 Stage 1- Boundary Definition

In the first stage of machine learning, the preliminary design space (consisting of all possible compositions with varying ratios of MXene, CNF, and gelatin) was screened in search of potentially viable design spaces. These feasible design spaces would then be used in the subsequent active learning stage so that the model could be trained to avoid the recipes with a high degree of failure. MXene aerogels were screened based on the observed continuity in the structure of the aerogels. The degree of continuity and the ability to form a freestanding 3D structure had been selected as the screening criteria because the samples needed to display some monolithic characteristics to be used in the mechanical test to generate data.

The aerogels were evaluated using a four-grade point scheme. The possible grades given to the aerogels are – 'A,' 'B,' 'C,' and 'D.' An 'A' grade sample represented a single freestanding monolithic MXene aerogel. Similarly, a 'B' grade was given to those samples that had visible cracks or split into large fragments but had maintained continuity in their structure with no sign of loose flakes. Likewise, a 'C' grade was given to samples with multiple fragments and some loose flakes. Lastly, the 'D' grade was for samples entirely formed of loose flakes and crumbles and could not form any continuous 3D structure fit for mechanical testing. Here, Figure 24. shows representative MXene aerogels for each grade.

continuous structure,
no multiple fragments

grade = A

mostly continuous structure,
but multiple fragments and cracks

grade = B

some continuity in structure,
presence of flakes

grade = C

very less continuity,
pronounced presence of flakes

grade = D

Figure 24. Showing MXene aerogel samples representing each grade point

Two hundred sixty-four (264) samples were prepared with all possible composition combinations at 10 wt.% intervals for four different mass-loadings (10 mg/ml, 7.5 mg/ml, 5 mg/ml, 2.5 mg/ml). The samples were prepared to conduct a grid search for the feasible design areas to produce viable MXene aerogels. The samples were graded following a double-blind observation. The grades were used as input points to train a support vector machine (SVM) classifier. After the SVM was trained, it produced a heat map with two regions within the preliminary design space showcasing areas with a high possibility of failure and success, as shown in Figure 25

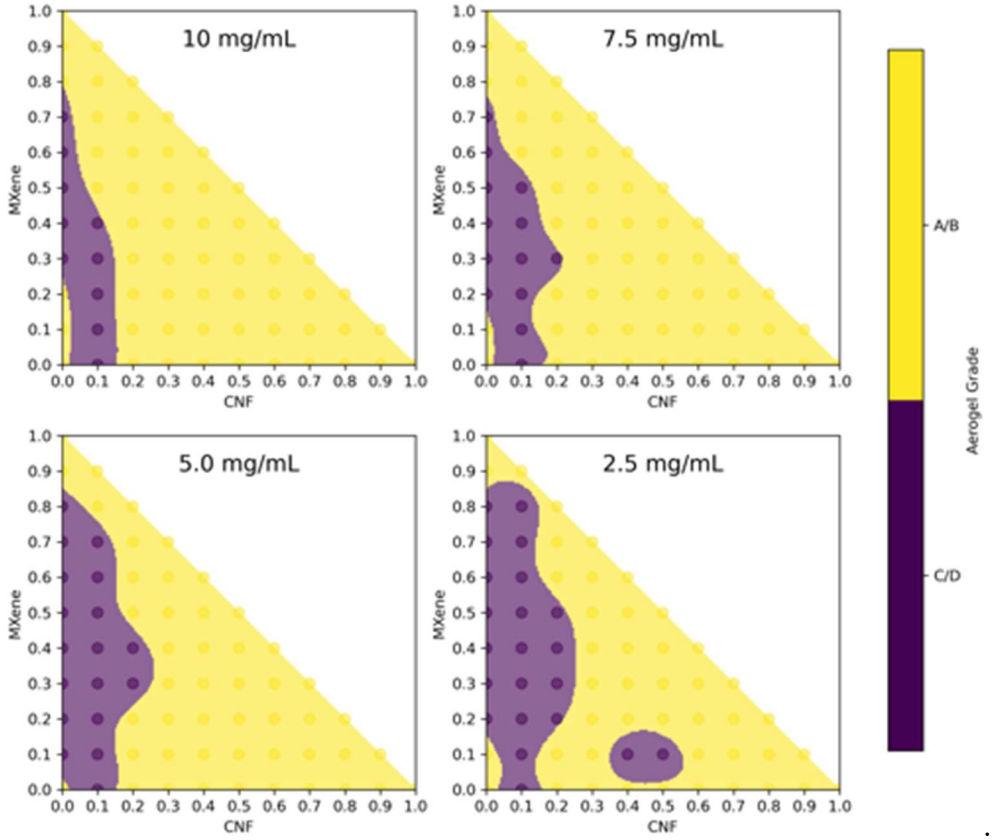

Figure 25. showing the heat maps produced by SVM for four different mass-loadings. Yellow-colored

region suggests possibility of high success for preparing near monolithic MXene aerogel samples. Similarly purple region signifies very low chances of making a freestanding monolithic aerogel

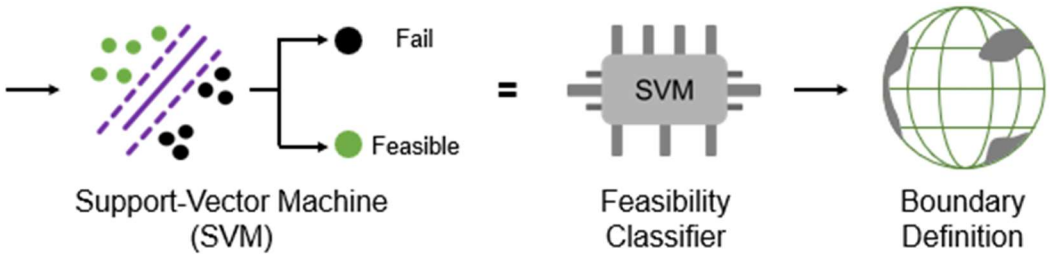

Figure 26. schematic illustration of an SVM classifier

The construction of an SVM classifier can be broken down into three fundamental steps. The first step in building an SVM classifier is to select a kernel function that will aid in learning and recognizing correlations of the data points. Secondly, data points are imported to train the SVM classifier and generate a heat map. Lastly, the SVM classifier is optimized to improve the accuracy of the heat map. The progression of SVM construction and its function is included in equation 1.

The SVM classifier in this study is optimized using Matthew's correlation coefficient (MCC)

$$MCC = \frac{TP \times TN - FP \times FN}{\sqrt{(TP+F\ )(TP+\ \ )(TN+FP)(TN+FN)}} \quad (1)$$

Here, TP, TN, FP, and FN mean true positive, true negative, false positive and false negative, respectively

4.3 Stage 2 – Active learning

Active learning is a dynamic process that uses repetitive learning methods to build up and mature the prediction models. The active learning process for this study

entailed generating data to train the model, evaluating the model, and exploring the feasible design space to further develop the model.

The active learning loops were initiated by selecting 30 random recipes to produce 30 random data points. Each datapoint consisted of nine different labels – four recipe labels (MXene ratio, CNF ratio, mass loading, cross-linker) representing the fabrication route, and five strain labels (ε_{15-L}, ε_{15-U}, ε_{25-L}, ε_{25-U}, ε_{30}) representing the sensor characteristics of the MXene aerogels (Figure 27).

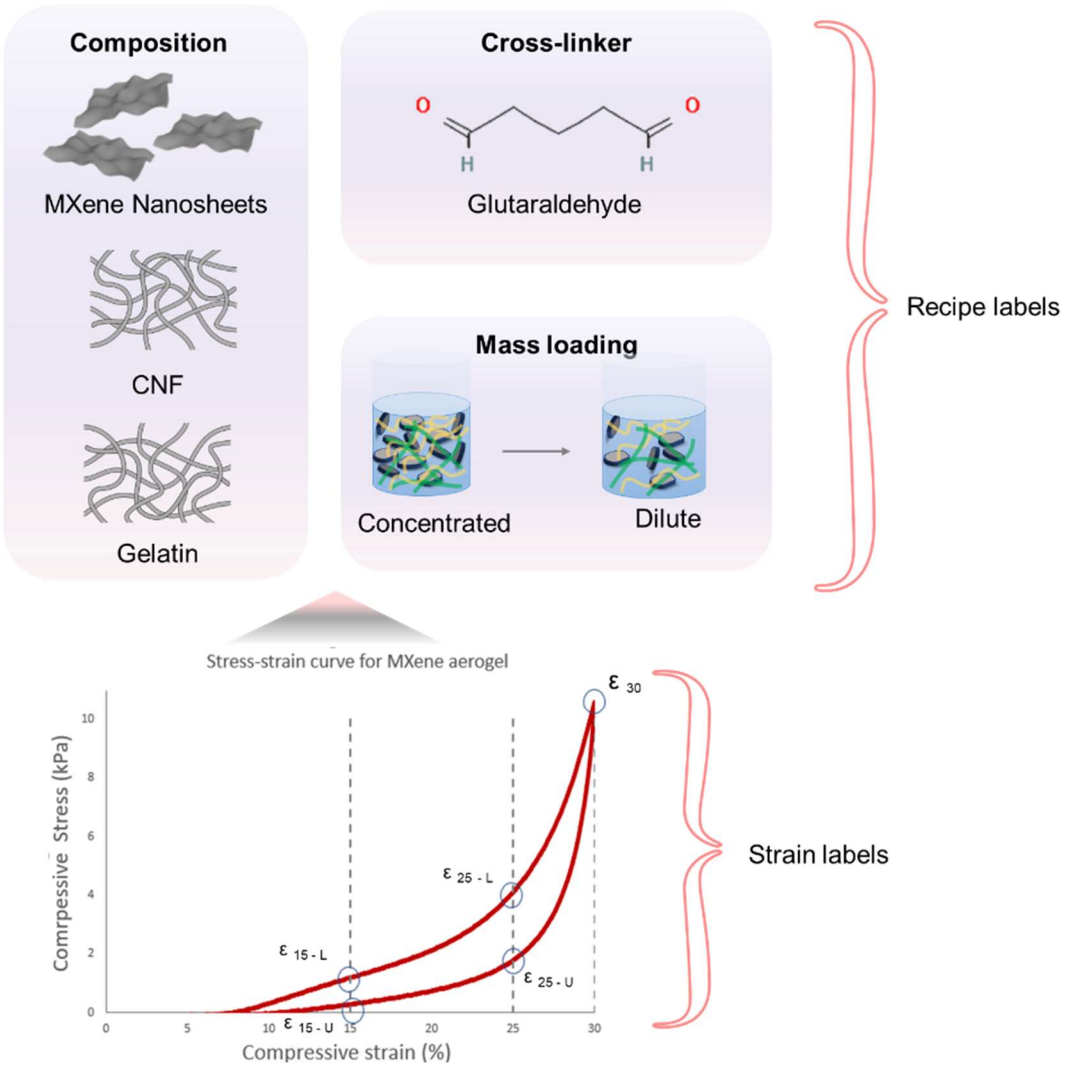

Figure 27. Showing schematic illustration of the 4 recipe labels (MXene ratio, CNF ratio, mass loading, cross-linker) representing fabrication route and 5 strain labels (ε 15 – L, ε 15 – U, ε 25 – L, ε 25 – U, ε 30) representing the sensor characteristics of MXene aerogels. The recipe labels in conjunction with the strain labels makes up a data point.

Then, the data points were input into the artificial neural network (ANN) and decision tree to train the decision programs. The decision programs were trained to predict the target data points' output values (strain labels of new recipes) for the next active learning round based on the previous data trend.

The acquisition function, A-scores, were calculated for all the targeted data points using the formula included in equation (2)

$$A - score = L_2 \times \widehat{\sigma} \quad (2)$$

Here, L_2 denotes the shortest mathematical distance between the current recipe labels and the targeted recipe label, while $\widehat{\sigma}$ signifies variance of the predicted output values for a given recipe label. The formula used in calculating L_2 and $\widehat{\sigma}$ are included in Equation 3 and 4, respectively.

Here, mx_i and cnf_i in equation (3) denote MXene ratio and CNF ratio of the recipes already included in the navigation model, while the "j" counterparts signify the recipe label of the targeted data points. 'N' represents the total number of decision programs used to generate the predictions. Similarly, in equation (4) variance of the predicted values obtained from the decision programs is calculated for each strain label.

The targeted values with the highest A-scores were selected for the next round of active learning. The mechanism behind an active learning loop is summarized and portrayed in Figure 28.

$$L_2 = \sqrt[2]{\min_{i \in N} \left[\left(\begin{bmatrix} mx_i \\ cnf_i \end{bmatrix} - \begin{bmatrix} mx_j \\ cnf_j \end{bmatrix} \right)^2 \right]} \quad (3)$$

$$\hat{\sigma} = \sqrt[2]{\frac{1}{N}\sum_{j=1}^{N} \left[\left(\begin{bmatrix} output^{j}_{\varepsilon 15-U} \\ output^{j}_{\varepsilon 15-L} \\ output^{j}_{\varepsilon 25-U} \\ output^{j}_{\varepsilon 25-L} \\ output^{j}_{\varepsilon 30} \end{bmatrix} - \begin{bmatrix} output^{ave}_{\varepsilon 15-U} \\ output^{ave}_{\varepsilon 15-L} \\ output^{ave}_{\varepsilon 25-U} \\ output^{ave}_{\varepsilon 25-L} \\ output^{ave}_{\varepsilon 30} \end{bmatrix} \right)^2 \right]} \quad (4)$$

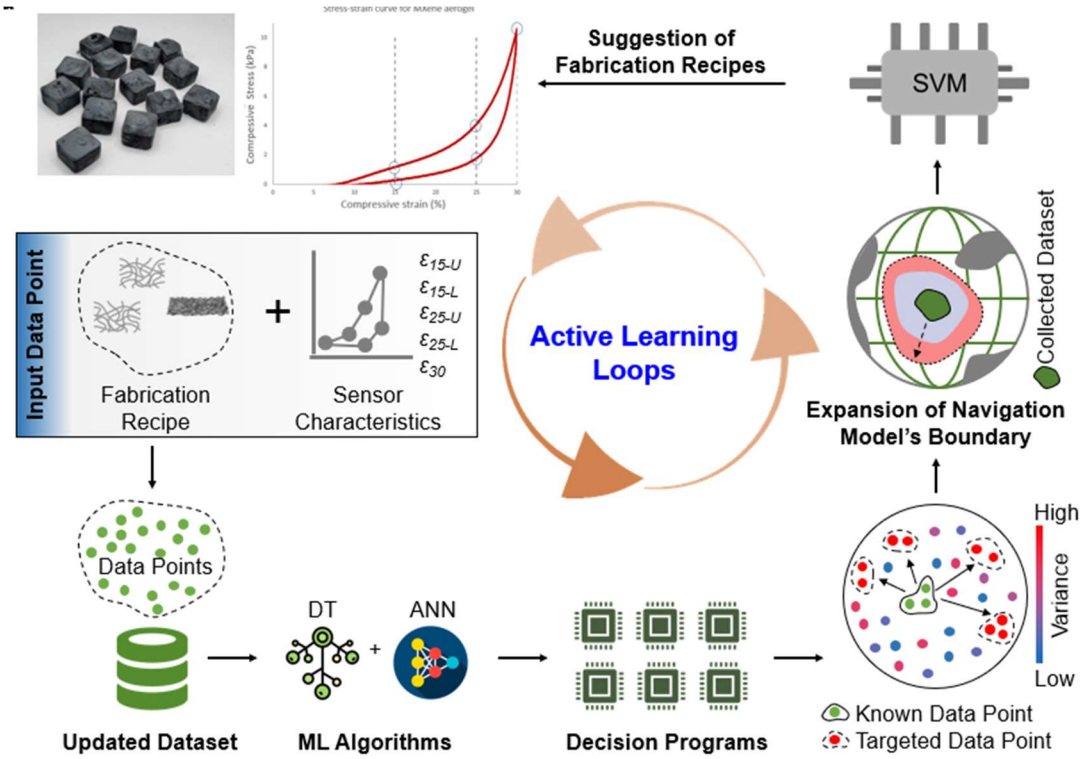

Figure 28. Showing schematic illustration of construction of a navigation model through active learning loops

So far, six active learning loops have been completed. The cumulative data points used in the construction of the current navigation model are shown in Figure 29. Similarly, Figures 30 and 31 show the prediction model for MXene aerogel fabrication developed after 6 loops of active learning for various recipe conditions.

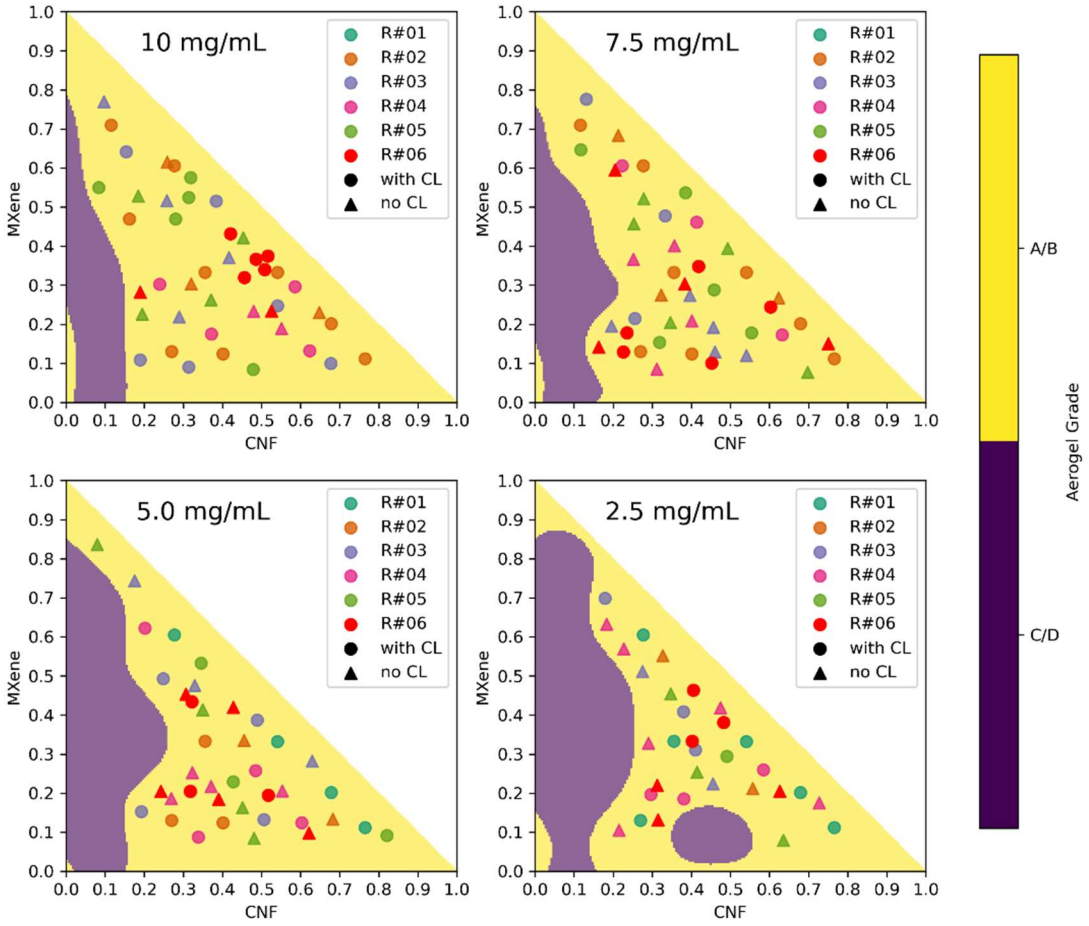

Figure 29. showing data points used to construct the navigation model through 6 active learning loops

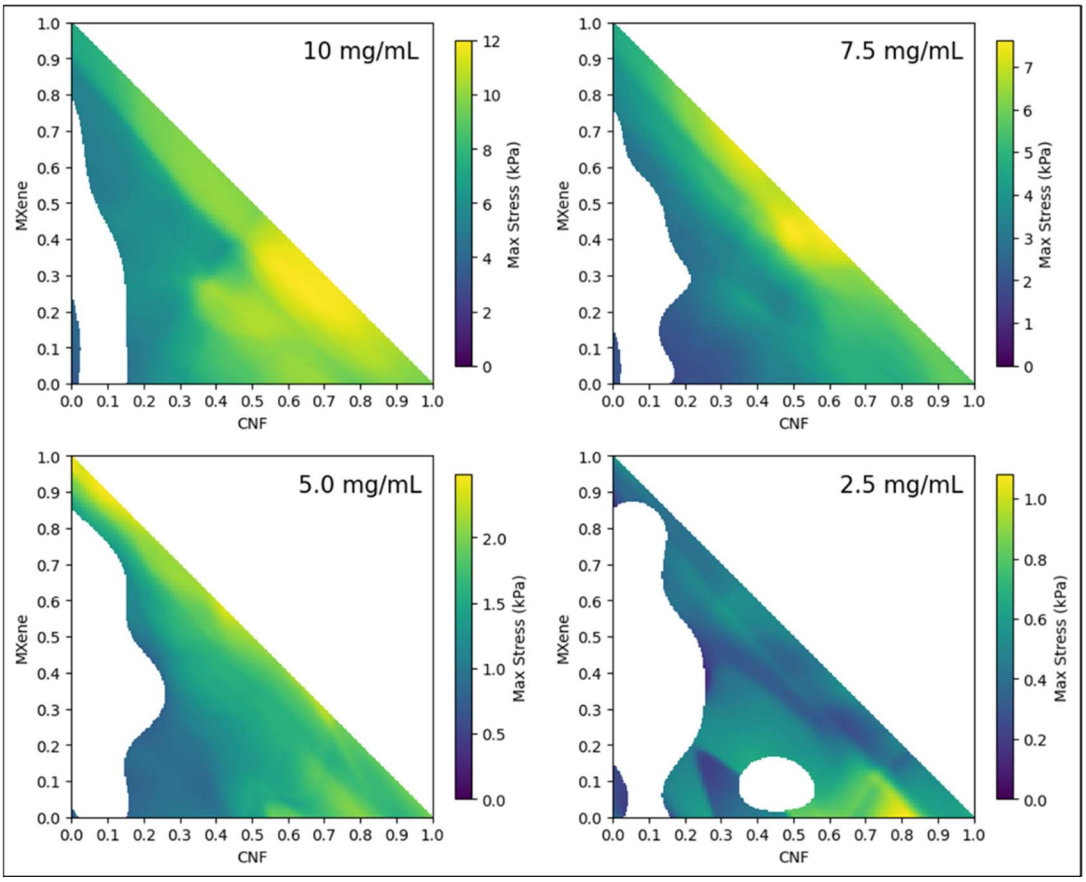

Figure 30. prediction model for MXene aerogel fabrication developed after six loops of active learning for the recipes with cross-linker

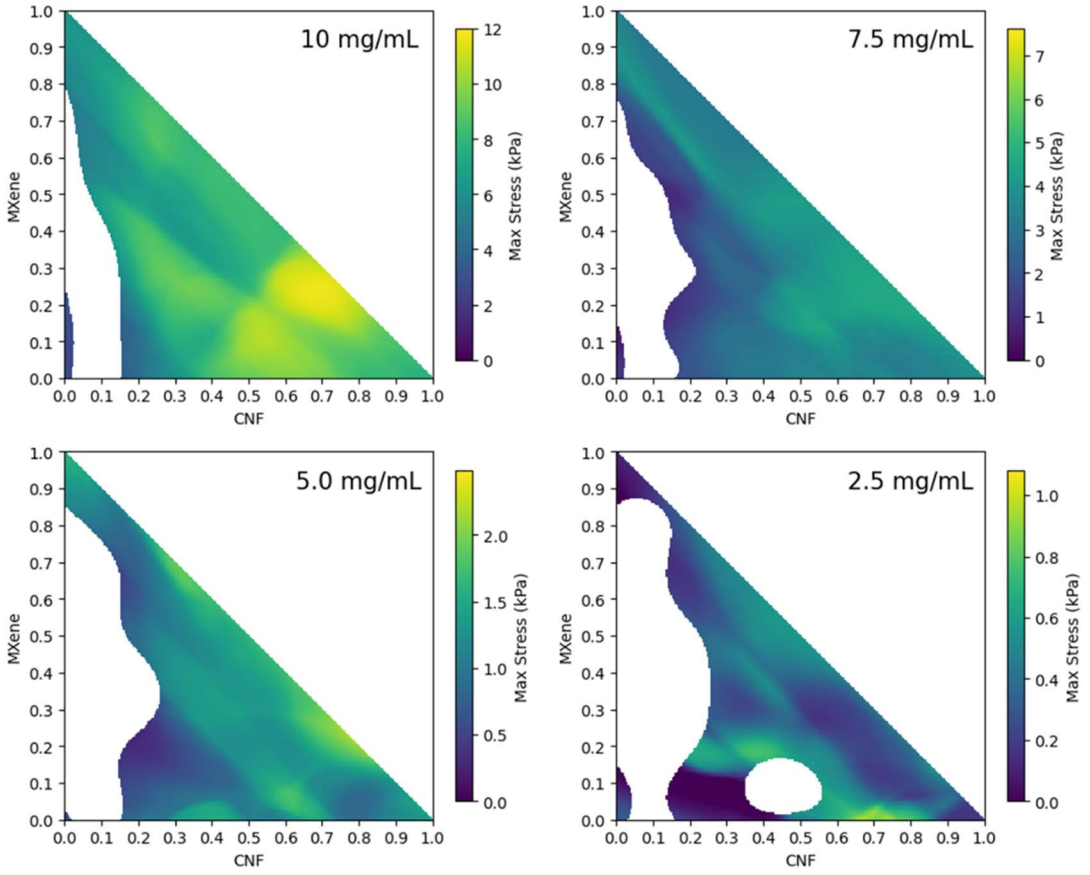

Figure 31. prediction model for MXene aerogel fabrication developed after six loops of active learning for the recipes without cross-linker

More tests need to be done to validate the prediction models. Mean squared error (MSE) obtained from the tests will determine if the active learning needs to be continued further. Active learning process is usually concluded as the MSE and $\bar{L}$ values stabilize. [53] MSE and $\bar{L}$ can be calculated using the formula in the equations (5) and (6). $\bar{L}$ is the average mathematical distance between the recipe labels for all the data points in the navigation model. $\bar{L}$ is the indicator of the exploration rate of the model.

$$MSE = \frac{1}{N}\sum_{i=1}^{N}\left(output^{i} - E^{i}\right)^{2} \quad (5)$$

$$\bar{L} = \frac{1}{N}\sum_{j=1}^{N}\left(\frac{1}{N}\sum_{i=1}^{N}\sqrt{\min_{i \in N}\left[\left(\begin{bmatrix} mx_i \\ cnf_i \end{bmatrix} - \begin{bmatrix} mx_j \\ cnf_j \end{bmatrix}\right)^{2}\right]}^{2}\right) \quad (6)$$

4.4 Stage 3 – Data augmentation

After the active learning cycles are completed, the prediction model will be further optimized using data augmentation. In the study done by Yang et al., data augmentation methods such as Synthetic Minority Oversampling Technique for Regression (SMOTE-REG) and User Input Principle (UIP) were used to augment data points from 125 to around 10,000. [53] The data augmentation step coupled with genetic algorithm (GA) selection was able to result in improved prediction models with the lowest MRE value measured at 24%.

Chapter 5: Data analysis

5.1 Statistical analysis

In addition to machine learning, statistical analysis was also performed to assess the non-linear correlation between the parameters using the Spearman rank correlation coefficient, abbreviated as Spearman's ρ. The value of Spearman's ρ can range from -1 to 1. There is a strong correlation between the output and input parameters if the absolute value of Spearman's ρ that is a higher value, and the p-value is $< 10^{-2}$

Based on the analysis (Figure 32), it was found that concentration/mass loading was the significant factor affecting the strength of MXene aerogel samples. Mass loading exhibits a positive correlation towards strength for most of the strain parameters of the aerogel.

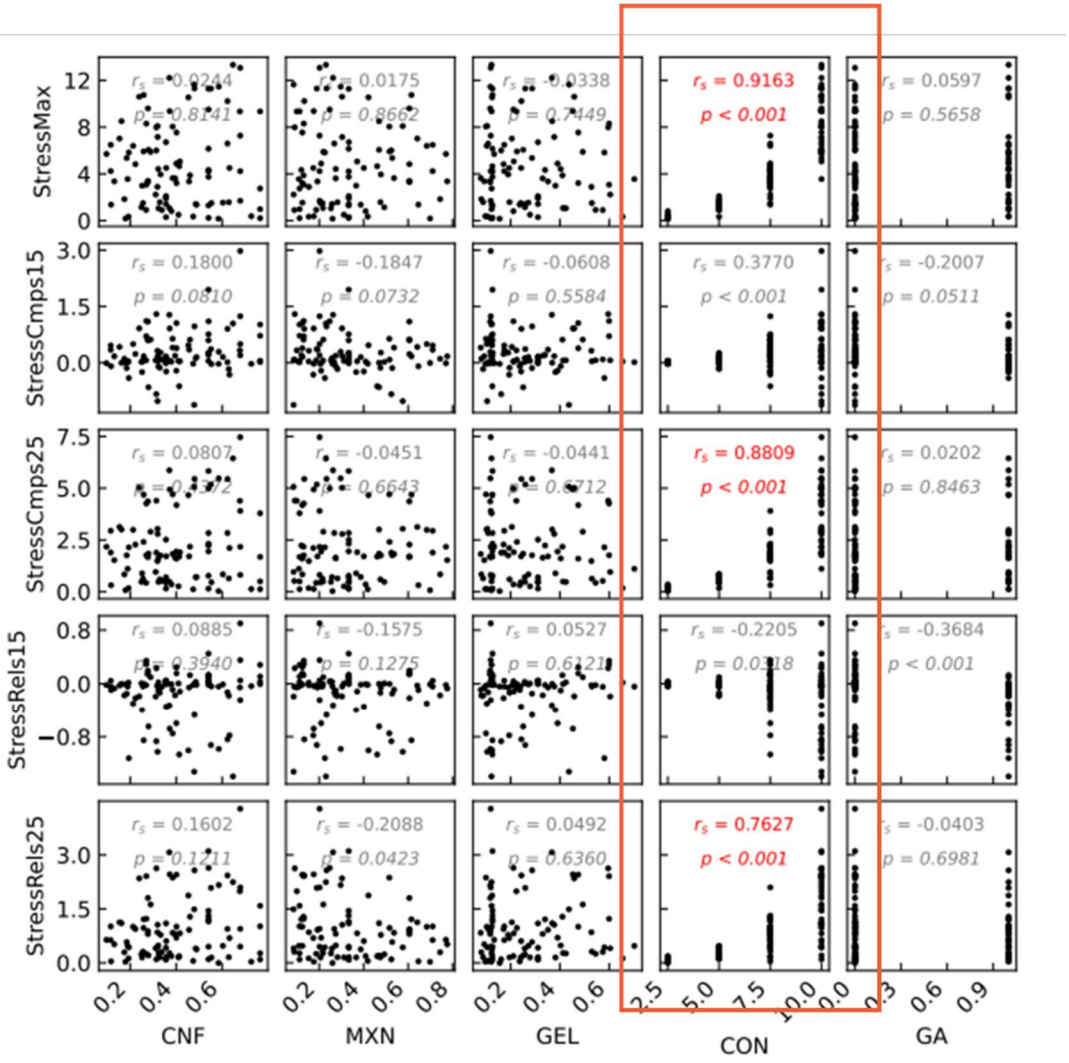

Figure 32. Spearman's ρ statistical analysis for all accumulated data points

Another observed correlation was CNF ratio and MXene aerogel strength for 10 mg/ml samples (Figure 33).

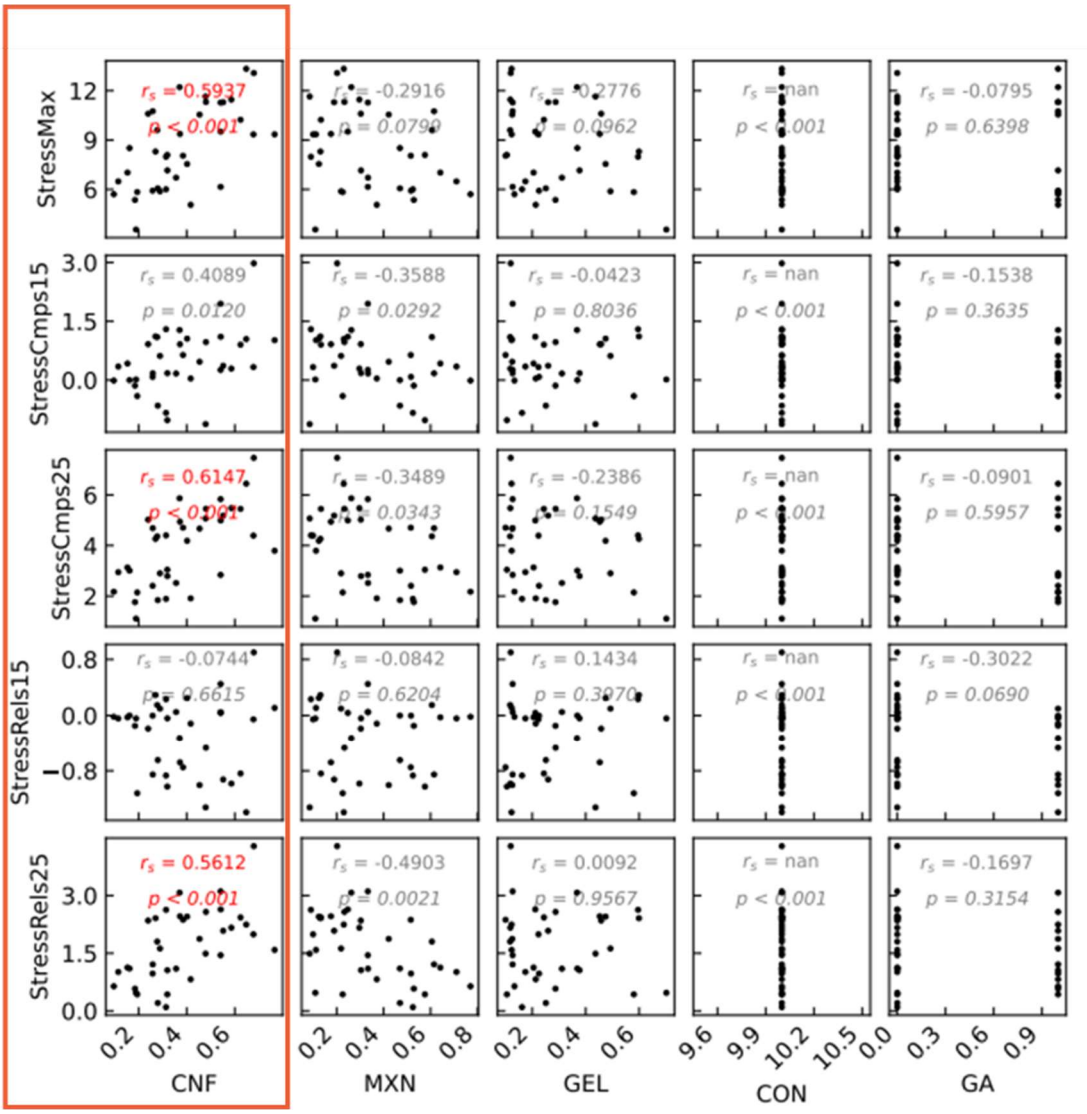

Figure 33. Spearman's ρ statistical analysis for all 10 mg/ml data points

5.2 Data Validation via mechanical results and electron microscopy

5.2.1 Data Validation via mechanical results

The observed mechanical performance of the MXene aerogel samples with the same recipe but with different mass loadings (Figure 34) agrees with the design principle discovered via Spearman's ρ analysis. In Figure 34, two sets of recipes are featured in graphs (A) and (B). Red, green, and blue curves in both the graphs represent the stress-strain curve for 10, 7.5, and 5 mg/ml, respectively. The corresponding SEM images of the MXene aerogel samples are presented in Figure. 31 for graph A and Figure 32 for graph B.

The drastic difference in the mechanical strength of the samples based on the mass loading suggests that mass loading has a prominent effect on the strength of the MXene aerogels, just as the correlation discovered in section 5.1.

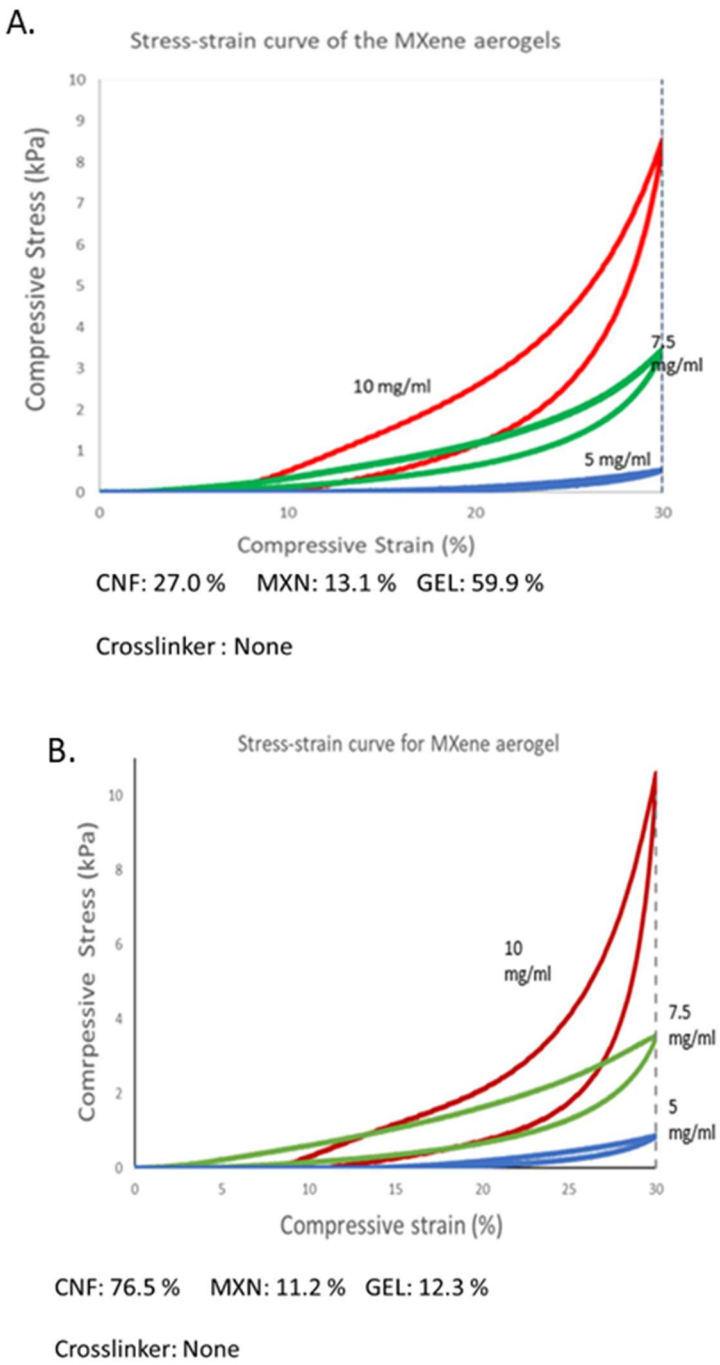

Figure 34. Graph showing compressive stress of three MXene aerogels with same recipe as shown in the figure, but with different mass loadings. Red curve is data for 10 mg/ml, green for 7.5 mg/ml and blue for 5 mg/ml

5.2.2 Data Validation via electron microscopy – Mass loading

Images via scanning electron microscopy (SEM) of some of the aerogel samples was taken to study their microstructures. SEM images in Figures 35 and 36 provide further validation of mass loading's influence on the mechanical properties of MXene aerogels. In Figure 35, the concentration of the aerogel sample decreases from top down . Both aerogel samples with 7.5 and 5 mg/ml mass loading Figure 35 have smaller and disordered microstructure. However, the microstructure of the 10 mg/ml sample forms a cellular, oriented, and nacre-like structure. This nacre like structure with brick and mortal layout has been widely discussed in the literature and is regarded as one of the factors in delivering high strength property to the material. [43,44] Interestingly, this observation is in agreement with compressive mechanical data from Figure 34 (Graph A).

Mass loading: 10 mg/ml

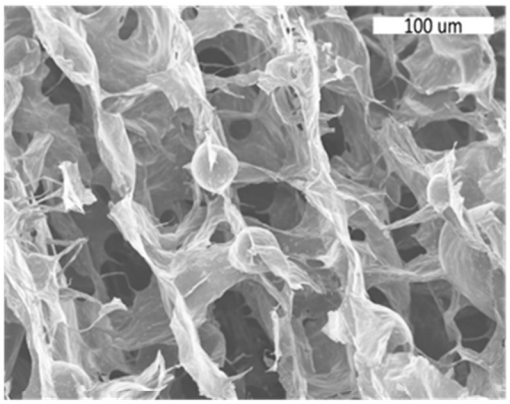

Mass loading: 7.5 mg/ml

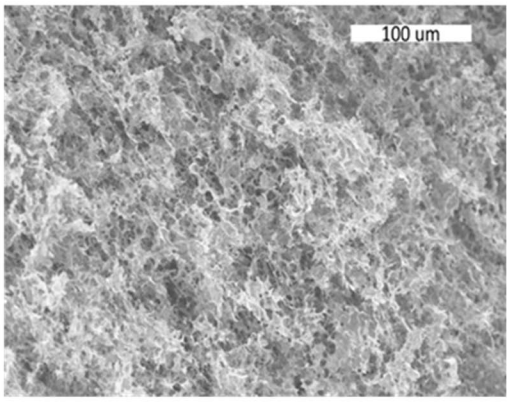

Mass loading: 5 mg/ml

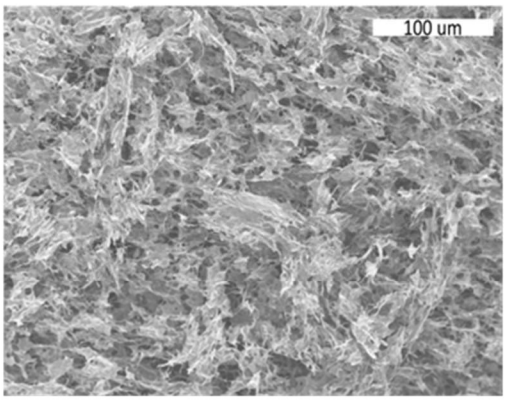

Recipe:

CNF: 27.0 % MXN: 13.1 % GEL: 59.9%

Crosslinker : None

Figure 35. SEM images showing the influence of mass loading in the microstructure of the MXene aerogel corresponding to the mechanical data of graph A in Figure. 34

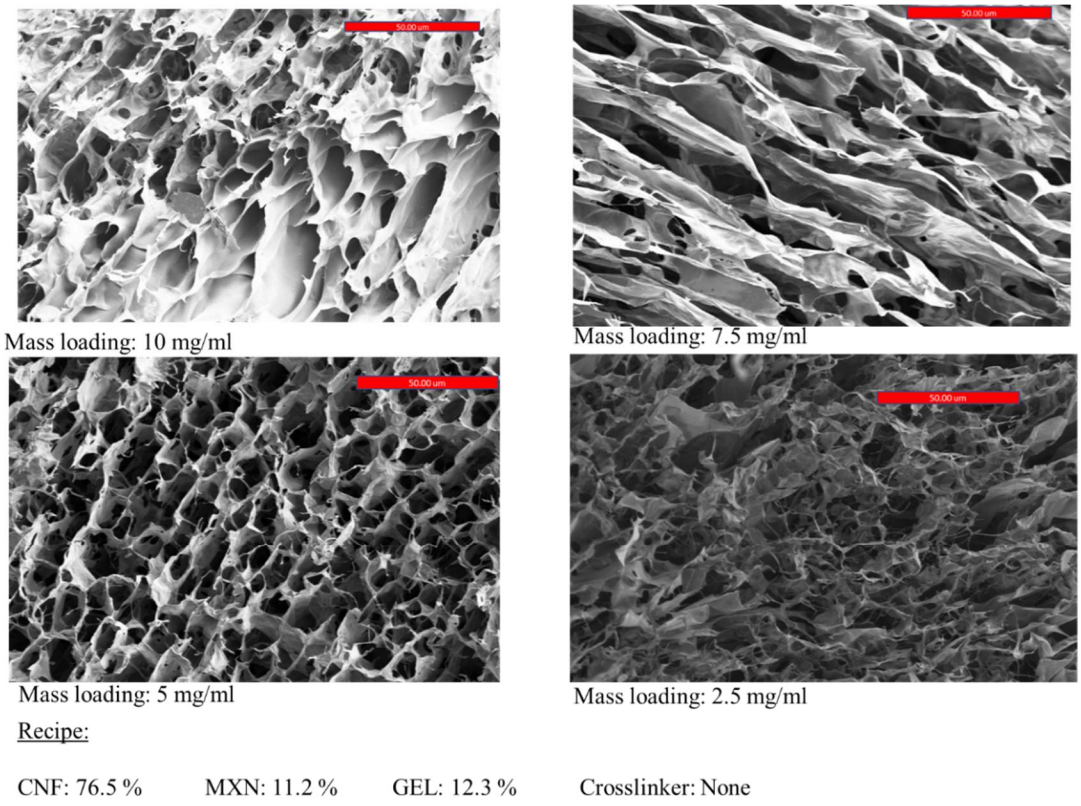

Figure 36. SEM images showing the influence of mass loading in the microstructure of the MXene aerogel corresponding to the mechanical data of graph B in Figure. 34

The progression in the difference of the microstructure of MXene aerogels in graph (B) does not match the trend observed in graph (A). And that is understandable as they are fabricated from two different recipes. All four samples exhibit some kind of cellular microstructure at the cross-section. However, upon closer inspection, it could be observed that the porosity and pore sizes increase gradually moving from top down with decreasing concentration. The apparent increase in porosity and the pore sizes can be used to explain the mechanical trend in the sample shown in Figure 34 (graph B), which exhibits a decrease in strength with decreasing concentration. As this observation is qualitative, Brunauer-Emmett-Teller (BET) measurement could be obtained in the future to gather quantitative data to support this claim.

5.2.3 Data Validation via electron microscopy – CNF ratio

Another correlation suggested by the statistical analysis using Spearman's ρ was the increase in the mechanical compressive strength of the MXene aerogels at 10 mg/ml with an increasing CNF ratio. Below in Figure 37, SEM images of three MXene aerogel samples prepared with 10 mg/ml mass loading are included. The CNF ratio of MXene aerogels in Figure 37 increases gradually from 0% to 20% and 40%. The corresponding SEM images show how the microstructure of the MXene aerogel samples evolved. The microstructure starts with being discontinuous with loosely connected flakes (Figure 37, A) for 0% CNF. The 20% CNF recipe MXene aerogel shows some cohesiveness in its microstructure with disordered random networks (Figure 37, B). And finally, MXene aerogel with 40% CNF exhibits a highly oriented and defined lamellar honeycomb structure (Figure 37, C).

A. **Composition**
CNF: 0 %
MXene: 60 %
Gelatin : 40 %

Concentration: 10 mg/ml

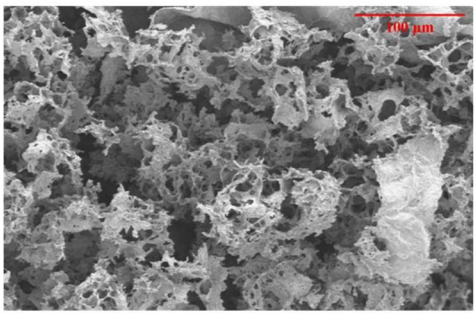

B. **Composition**
CNF: 20 %
MXene: 30 %
Gelatin : 50 %

Concentration: 10 mg/ml

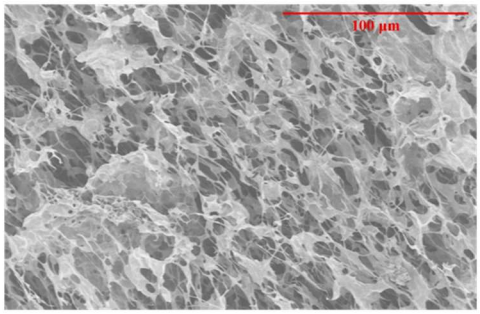

C. **Composition**
CNF: 40 %
MXene: 60 %
Gelatin : 0 %

Concentration: 10 mg/ml

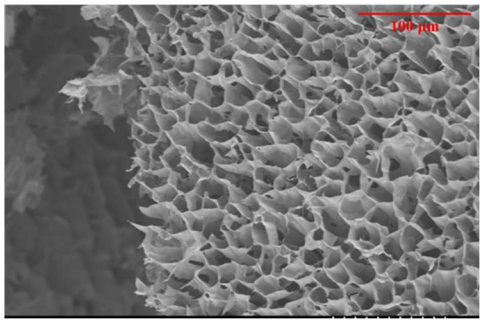

Figure 37. SEM images showing the influence of CNF ratio in the microstructure of the MXene aerogels

Chapter 6: Conclusion

This study was inspired by the innovative approach used by Yang et al., which used machine learning to navigate a complex design space consisting of multiple correlating factors. Here, a similar machine learning framework was adopted to explore an equally complicated design landscape with multiple degrees of freedom. Fabrication of MXene aerogels for piezoresistive sensors involved 4 degrees of freedom, with 2 degrees of freedom from composition, one from concentration, and one from the addition of the cross-linker. A trial-and-error method through the grid search of the entire design space would have been tremendously inefficient and virtually impossible, given the number of experiments that need to be completed for a comprehensive analysis. Therefore, following the example set by Yang et al., a hybrid strategy was implemented using machine learning in conjunction with experimental studies to uncover the core design principles.

In the first stage of the machine learning framework, a grid search of 2-D design space based only on the composition was conducted as a preliminary screening to determine the feasible design spaces. Two hundred sixty-four aerogels were fabricated to train the SVM classifier to produce a continuous heat map defining feasible design regions. Robotic collaboration was incorporated for high-throughput automated screening via OT-2 pipetting robot to assemble the building block for the fabrication and UR5e robotic arm for compressive testing to maintain a data-rich system and streamline the process. Six rounds of active learning cycles have been completed with

the current navigation model consisting of 160 data points. A couple of ML-enabled prediction models have been developed.

For future studies, $\bar{L}$ and MSE values will be calculated to determine the conclusion of active learning stage. The models will be optimized using data augmentation via virtual data points. After that, design principles will be validated through additional tests.

Additionally, statistical analysis was also conducted using the Spearman rank correlation coefficient (Spearman's ρ) to assess any non-linear correlations between the input and output parameters. It was discovered that mass loading had the most dominating influence on the strength of the aerogel. This design principle was further validated when compressive mechanical tests were compared for the two sets of MXene aerogels made from the same fabrication recipe but with different concentrations. SEM images of the corresponding aerogel samples gave additional evidence on the microstructural level, which shows an increase in pore sizes with decreasing concentration or an increase in structural order with increasing concentration. Similarly, another influential factor discovered from the statistical analysis was the ratio of CNF for aerogel samples of 10 mg/ml mass loading. BET measurement will be conducted to obtain a more concrete validation in future studies.

Bibliography

1. Tan, C.; Cao, X.; Wu, X.-J.; He, Q.; Yang, J.; Zhang, X.; Chen, J.; Zhao, W.; Han, S.; Nam, G.-H.; Sindoro, M.; Zhang, H. Recent Advances in Ultrathin Two-Dimensional Nanomaterials. *Chem. Rev.***2017**, *117* (9), 6225–6331.
2. Tiwari, S. K.; Sahoo, S.; Wang, N.; Huczko, A. Graphene Research and Their Outputs: Status and Prospect. *J SCI-ADV MATER DEV* **2020**, *5* (1), 10–29.
3. Geim, A. K.; Novoselov, K. S. The Rise of Graphene.
4. Hu, T.; Mei, X.; Wang, Y.; Weng, X.; Liang, R.; Wei, M. Two-Dimensional Nanomaterials: Fascinating Materials in Biomedical Field. *Sci. Bull.* **2019**, *64* (22), 1707–1727.
5. Gong, K.; Zhou, K.; Qian, X.; Shi, C.; Yu, B. MXene as Emerging Nanofillers for High-Performance Polymer Composites: A Review. *Compos. B. Eng.* **2021**, *217*, 108867.
6. Gogotsi, Y.; Anasori, B. The Rise of MXenes. *ACS Nano*. 2019.
7. Shuck, C. E.; Gogotsi, Y. MXenes: A tunable family of 2D carbides and Nitrides. Millipore Sigma. https://www.sigmaaldrich.com/US/en/technical-documents/technical-article/materials-science-and-engineering/organic-electronics/mxenes
8. Gonzalez-Julian, J. Processing of MAX Phases: From Synthesis to Applications. *J. Am. Ceram. Soc.* **2021**, *104* (2), 659–690.

9. Alnoor, H.; Elsukova, A.; Palisaitis, J.; Persson, I.; Tseng, E. N.; Lu, J.; Hultman, L.; Persson, P. O. Å. Exploring MXenes and Their MAX Phase Precursors by Electron Microscopy. *Mater. Today Adv.* **2021**, *9*, 100123.
10. Ronchi, R. M.; Arantes, J. T.; Santos, S. F. Synthesis, Structure, Properties and Applications of MXenes: Current Status and Perspectives. *Ceram. Int.* **2019**, *45* (15), 18167–18188.
11. Naguib, M.; Barsoum, M. W.; Gogotsi, Y. Ten Years of Progress in the Synthesis and Development of MXenes. *Adv. Mater.* **2021**, *33* (39), 2103393.
12. Randviir, E. P.; Brownson, D. A. C.; Banks, C. E. A Decade of Graphene Research: Production, Applications and Outlook. *Mater. Today* **2014**, *17* (9), 426–432.
13. Lipatov, A.; Lu, H.; Alhabeb, M.; Anasori, B.; Gruverman, A.; Gogotsi, Y.; Sinitskii, A. Elastic Properties of 2D $Ti_3C_2T_x$ MXene Monolayers and Bilayers. *Sci. Adv.* **2018**, *4* (6), eaat0491.
14. Anasori, B.; Lukatskaya, M. R.; Gogotsi, Y. 2D Metal Carbides and Nitrides (MXenes) for Energy Storage. *Nat. Rev. Mater.* **2017**, *2* (2), 16098.
15. Vladislav, K.; S, F. A.; Huicheng, H.; Xue, R.; Francisco, L.; Di, W.; F, K. R.; V, T. D. Covalent Surface Modifications and Superconductivity of Two-Dimensional Metal Carbide MXenes. *Science (1979)* **2020**, *369* (6506), 979–983.
16. Naguib, M.; Mochalin, V. N.; Barsoum, M. W.; Gogotsi, Y.; Naguib, M.; Mochalin, V. N.; Barsoum, M. W.; Gogotsi, Y. Anniversary Article: MXenes:

A New Family of Two-Dimensional Materials. *Adv. Mater* **2014**, *26*, 992–1005.

17. Urbankowski, P., Anasori, B., Hantanasirisakul, K., Yang, L., Zhang, L., Urbankowski, P.; Anasori, B.; Hantanasirisakul, K.; Yang, L.; Zhang, L.; Haines, B.; May, S. J.; L Billinge, S. J.; Gogotsi, Y. 2D Molybdenum and Vanadium Nitrides Synthesized by Ammoniation of 2D Transition Metal Carbides (MXenes) †. *Nanoscale* **2017**, *9*, 17722.
18. Tang, X.; Guo, X.; Wu, W.; Wang, G. 2D Metal Carbides and Nitrides (MXenes) as High-Performance Electrode Materials for Lithium-Based Batteries.
19. Sang, X.; Xie, Y.; Lin, M.-W.; Alhabeb, M.; van Aken, K. L.; Gogotsi, Y.; Kent, P. R. C.; Xiao, K.; Unocic, R. R. Atomic Defects in Monolayer Titanium Carbide (Ti3C2Tx) MXene. *ACS Nano* **2016**, *10* (10), 9193–9200.
20. Ling, Z.; Ren, C. E.; Zhao, M.-Q.; Yang, J.; Giammarco, J. M.; Qiu, J.; Barsoum, M. W.; Gogotsi, Y. Flexible and Conductive MXene Films and Nanocomposites with High Capacitance. *Proc. Natl. Acad. Sci.* **2014**, *111* (47), 16676–16681.
21. Chen, H.; Müller, M. B.; Gilmore, K. J.; Wallace, G. G.; Li, D. Mechanically Strong, Electrically Conductive, and Biocompatible Graphene Paper. *Adv. Mater.* **2008**, *20* (18), 3557–3561.
22. Zhao, M.-Q.; Zhang, Q.; Huang, J.-Q.; Tian, G.-L.; Nie, J.-Q.; Peng, H.-J.; Wei, F. ARTICLE Unstacked Double-Layer Templated Graphene for High-Rate Lithium-Sulphur Batteries. *Nat. Commun.* **2014**.

23. Plummer, G.; Anasori, B.; Gogotsi, Y.; Tucker, G. J. Nanoindentation of Monolayer Tin+1CnTx MXenes via Atomistic Simulations: The Role of Composition and Defects on Strength. *Comput. Mater. Sci.***2019**, *157*, 168–174.

24. Lee, C.; Wei, X.; Kysar, J. W.; Hone, J. Measurement of the Elastic Properties and Intrinsic Strength of Monolayer Graphene. *Science (1979)* **2008**, *321* (5887), 385–388.

25. Suk, J. W.; Piner, R. D.; An, J.; Ruoff, R. S. Mechanical Properties of Monolayer Graphene Oxide. *ACS Nano* **2010**, *4* (11), 6557–6564.

26. Li, X.; Zhu, Y.; Cai, W.; Borysiak, M.; Han, B.; Chen, D.; Piner, R. D.; Colombo, L.; Ruoff, R. S. Transfer of Large-Area Graphene Films for High-Performance Transparent Conductive Electrodes. *Nano Lett.* **2009**, *9* (12), 4359–4363.

27. Zhang, N.; Hong, Y.; Yazdanparast, S.; Asle Zaeem, M. Superior Structural, Elastic and Electronic Properties of 2D Titanium Nitride MXenes over Carbide MXenes: A Comprehensive First Principles Study. *2d Mater.* **2018**, *5* (4), 045004.

28. Borysiuk, V. N.; Mochalin, V. N.; Gogotsi, Y. Bending Rigidity of Two-Dimensional Titanium Carbide (MXene) Nanoribbons: A Molecular Dynamics Study. *Comput. Mater. Sci.* **2018**, *143*, 418–424.

29. Natu, V.; Sokol, M.; Verger, L.; Barsoum, M. W. Effect of Edge Charges on Stability and Aggregation of Ti 3 C 2 T z MXene Colloidal Suspensions. **2018**.

30. Shekhirev, M.; Shuck, C. E.; Sarycheva, A.; Gogotsi, Y. Characterization of MXenes at Every Step, from Their Precursors to Single Flakes and Assembled Films. *Prog. Mater. Sci*. **2021**, *120*, 100757.

31. Trung, T. Q.; Lee, N.-E. Flexible and Stretchable Physical Sensor Integrated Platforms for Wearable Human-Activity Monitoring and Personal Healthcare. *Adv. Mater.* **2016**, *28* (22), 4338–4372.

32. Ma, C.; Ma, M.-G.; Si, C.; Ji, X.-X.; Wan, P. Flexible MXene-Based Composites for Wearable Devices. *Adv. Funct. Mater.* **2021**, *31* (22), 2009524.

33. Shi, X.; Fan, X.; Zhu, Y.; Liu, Y.; Wu, P.; Jiang, R.; Wu, B.; Wu, H.-A.; Zheng, H.; Wang, J.; Ji, X.; Chen, Y.; Liang, J. Pushing Detectability and Sensitivity for Subtle Force to New Limits with Shrinkable Nanochannel Structured Aerogel. *Nat. Commun.* **2022**, *13* (1), 1119.

34. Li, Y.; Chen, Y.; Yang, Y.; Wei, Y. Passive Particle Jamming and Its Stiffening of Soft Robotic Grippers. *IEEE Trans. Robot.* **2017**, *33* (2).

35. Alshareef, H. N.; Zhang, Y.-Z.; El-Demellawi, J. K.; Jiang, Q.; Ge, G.; Liang, H.; Lee, K.; Dong. MXene Hydrogels: Fundamentals and Applications. *Chem. Soc. Rev* **2020**, *49*, 7229.

36. Yao, L.; Gu, Q.; Yu, X. Three-Dimensional MOFs@MXene Aerogel Composite Derived MXene Threaded Hollow Carbon Confined CoS Nanoparticles toward Advanced Alkali-Ion Batteries. *ACS Nano* **2021**, *15* (2), 3228–3240.

37. Rafieerad, A.; Sequiera, G. L.; Yan, W.; Kaur, P.; Amiri, A.; Dhingra, S. Sweet-MXene Hydrogel with Mixed-Dimensional Components for Biomedical Applications. *J Mech Behav Biomed Mater* **2020**, *101*, 103440.

38. Ding, G.; Yang, B.; Chen, R.-S.; Zhou, K.; Han, S.-T.; Zhou, Y. MXenes for Memristive and Tactile Sensory Systems. *Appl. Phys. Rev.* **2021**, *8* (1), 011316.

39. Heikenfeld, C. J.; Rogers, J.; Pan, T.; Khine, M.; Wang, J.; Heikenfeld, J.; Jajack, A.; Gutruf, bg P.; Tian, L.; Li, R.; Kim, J. Lab on a Chip Devices and Applications at the Micro-and Nanoscale Lab on a Chip Wearable Sensors: Modalities, Challenges, and Prospects. *Lab Chip 18*, 217.

40. Quero, F.; Rosenkranz, A. Mechanical Performance of Binary and Ternary Hybrid MXene/Nanocellulose Hydro- and Aerogels – A Critical Review. *Adv. Mater. Interfaces* **2021**, *8* (18), 2100952.

41. Qin, L.; Yang, D.; Zhang, M.; Zhao, T.; Luo, Z.; Yu, Z. Z. Superelastic and Ultralight Electrospun Carbon Nanofiber/MXene Hybrid Aerogels with Anisotropic Microchannels for Pressure Sensing and Energy Storage. *J. Colloid Interface Sci.* **2021**, *589*, 264–274.

42. Wang, L.; Zhang, M.; Yang, B.; Tan, J.; Ding, X. Highly Compressible, Thermally Stable, Light-Weight, and Robust Aramid Nanofibers/Ti3AlC2 MXene Composite Aerogel for Sensitive Pressure Sensor. *ACS Nano* **2020**, *14* (8), 10633–10647.

43. Su, T.; Liu, N.; Gao, Y.; Lei, D.; Wang, L.; Ren, Z.; Zhang, Q.; Su, J.; Zhang, Z. MXene/Cellulose Nanofiber-Foam Based High Performance Degradable

Piezoresistive Sensor with Greatly Expanded Interlayer Distances. *Nano Energy* **2021**, *87*, 106151.

44. Zeng, Z.; Wang, C.; Siqueira, G.; Han, D.; Huch, A.; Abdolhosseinzadeh, S.; Heier, J.; Nüesch, F.; Zhang, C.; Nyström, G.; Zeng, Z.; Siqueira, G.; Huch, A.; Nyström, G.; Wang, C.; Han, D.; Zurich Zürich, in; Abdolhosseinzadeh, S. S.; Heier, J.; Nüesch, F.; Zhang, C.; Abdolhosseinzadeh, S. Nanocellulose-MXene Biomimetic Aerogels with Orientation-Tunable Electromagnetic Interference Shielding Performance. *Adv. Sci* **2000**, *2020*.
45. de France, K. J.; Hoare, T.; Cranston, E. D. Review of Hydrogels and Aerogels Containing Nanocellulose. **2017**.
46. Jiang, Y., Xv, X., Liu, D., Yang, Z., Zhang, Q., Shi, H., Zhao, G., and Zhou, J. (2018). Preparation of cellulose nanofiber-reinforced gelatin hydrogel and optimization for 3D printing applications**,** *BioRes.* 13(3), 5909-5924.
47. Jeon, J. G.; Kim, H. C.; Palem, R. R.; Kim, J.; Kang, T. J. Cross-Linking of Cellulose Nanofiber Films with Glutaraldehyde for Improved Mechanical Properties. *Mater. Lett.* **2019**, *250*, 99–102.
48. Yin, O. S.; Ahmad, I.; Amin, Mohd. C. I. M. Synthesis of Chemical Cross-Linked Gelatin Hydrogel Reinforced with Cellulose Nanocrystals (CNC). *AIP Conf Proc* **2014**, *1614* (1), 375–380.
49. Bigi, A.; Cojazzi, G.; Panzavolta, S.; Rubini, K.; Roveri, N. Mechanical and Thermal Properties of Gelatin Films at Different Degrees of Glutaraldehyde Crosslinking. *Biomaterials* **2001**, *22* (8), 763–768.

50. Li, S.; Chang, T.-H.; Li, Y.; Ding, M.; Yang, J.; Chen, P.-Y. Stretchable Ti3C2Tx MXene Microsupercapacitors with High Areal Capacitance and Quasi-Solid-State Multivalent Neutral Electrolyte. *J. Mater. Chem* **2021**, *9* (8), 4664–4672.
51. National Center for Biotechnology Information (2022). PubChem Compound Summary for CID 3485, Glutaraldehyde.
52. *Science of Fruit Jellies*. Experiments | Naked Scientists. (n.d.). https://www.thenakedscientists.com/get-naked/experiments/science-fruit-jellies.
53. Yang, H.; Li, J.; Lim, K. Z.; Pan, C.; van Truong, T.; Wang, Q.; Li, K.; Li, S.; Xiao, X.; Ding, M.; Chen, T.; Liu, X.; Xie, Q.; Alvarado, P. V. y.; Wang, X.; Chen, P.-Y. Automatic Strain Sensor Design via Active Learning and Data Augmentation for Soft Machines. *Nature Machine Intelligence* **2022**, *4* (1), 84–94.
54. Cao, B., Adutwum, L. A., Oliynyk, A. O., Luber, E. J., Olsen, B. C., Mar, A., & Buriak, J. M. (2018). How To Optimize Materials and Devices via Design of Experiments and Machine Learning: Demonstration Using Organic Photovoltaics. *ACS Nano*, *12*, 5.
55. Burchell, M. J., Armes, S. P., Fielding, L. A., & Hillier, J. K. (n.d.). ChemComm Chemical Communications Space science applications for conducting polymer particles: synthetic mimics for cosmic dust and micrometeorites Space science applications for conducting polymer particles:

synthetic mimics for cosmic dust and micrometeorites. *Chem. Commun*, *51*, 16886.

56. Cai, C.; Wei, Z.; Huang, Y.; Fu, Y. Wood-Inspired Superelastic MXene Aerogels with Superior Photothermal Conversion and Durable Superhydrophobicity for Clean-up of Super-Viscous Crude Oil. *Chemical Engineering Journal* **2021**, *421*, 127772.